



## Effect of composition and preparation of supported MoO<sub>3</sub> catalysts for anisole hydrodeoxygenation



Chanakya Ranga<sup>a</sup>, Rune Lødeng<sup>b</sup>, Vaios I. Alexiadis<sup>a</sup>, Tapas Rajkhowa<sup>a</sup>, Hilde Bjørkan<sup>b</sup>, Svatopluk Chytil<sup>b</sup>, Ingeborg H. Svenum<sup>c</sup>, John Walmsley<sup>c</sup>, Christophe Detavernier<sup>d</sup>, Hilde Poelman<sup>a</sup>, Pascal Van Der Voort<sup>e</sup>, Joris W. Thybaut<sup>a,\*</sup>

<sup>a</sup> Laboratory for Chemical Technology, Ghent University, Technologiepark, 914, B-9052 Ghent, Belgium

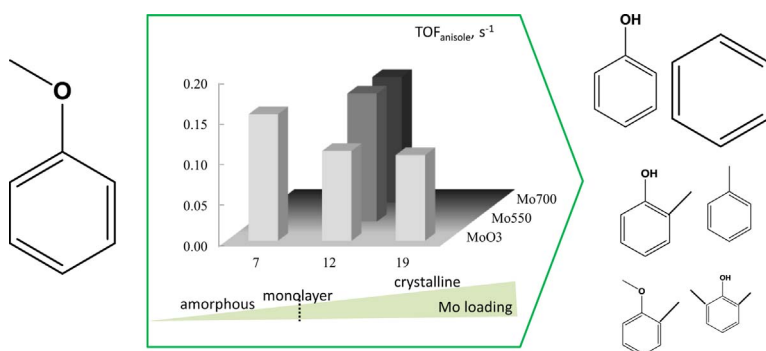
<sup>b</sup> SINTEF Materials and Chemistry, Kinetics and Catalysis Research Team, N-7465 Trondheim, Norway

<sup>c</sup> SINTEF Materials and Chemistry, Materials Physics Research Team, N-7465 Trondheim, Norway

<sup>d</sup> Department of Solid State Sciences, Ghent University, Krijgslaan 281/S1, B-9000 Ghent, Belgium

<sup>e</sup> Department of Inorganic and Physical Chemistry, Ghent University, Krijgslaan 281/S3, B-9000 Ghent, Belgium

### GRAPHICAL ABSTRACT



### ARTICLE INFO

#### Keywords:

Bio-oil  
Hydrodeoxygenation  
Gas phase  
Anisole  
Molybdenum oxide  
Reaction pathway

### ABSTRACT

A series of zirconia supported molybdenum oxide materials with Mo loadings of 7, 12, and 19 wt% were synthesized using incipient wetness impregnation. The as synthesized oxide materials were further modified under H<sub>2</sub>/CH<sub>4</sub> (80/20%, v/v) at 550 and 700 °C. The obtained catalysts were characterized by ICP-OES, XRD, Raman spectroscopy, H<sub>2</sub>-TPR, NH<sub>3</sub>-TPD, XPS, (S)TEM-EDX, BET, CHNS and CO chemisorption. While the Mo species, i.e., MoO<sub>3</sub> and Zr(MoO<sub>4</sub>)<sub>2</sub>, in the 7 wt% Mo loaded material were found to be of rather amorphous nature, their crystallinity increased significantly with Mo loading. The anisole hydrodeoxygenation performance of the catalysts was evaluated at gas phase conditions in a fixed bed tubular reactor in plug flow regime. A predominant selectivity towards hydrodeoxygenation and methyl transfer reactions rather than to hydrogenation was observed, irrespective of the Mo loading and further treatment, yet interesting differences in activity were observed. The highest anisole conversion was obtained on the catalyst(s) with 12% Mo loading, while the 7% Mo loaded one(s) exhibited the highest turnover frequency (TOF<sub>anisole</sub>) of 0.15 s<sup>-1</sup>. CO chemisorption, XPS analysis and kinetic measurements indicate that treatment under H<sub>2</sub>/CH<sub>4</sub> slightly reduced the initial anisole conversion, yet enhanced catalyst stability as well as TOF, probably due to the increased amounts of Mo<sup>5+</sup> species. The

\* Corresponding author.

E-mail address: [Joris.Thybaut@UGent.be](mailto:Joris.Thybaut@UGent.be) (J.W. Thybaut).

<http://dx.doi.org/10.1016/j.cej.2017.10.090>

Received 8 April 2017; Received in revised form 6 October 2017; Accepted 16 October 2017

Available online 17 October 2017

1385-8947/ © 2017 The Authors. Published by Elsevier B.V. This is an open access article under the CC BY-NC-ND license (<http://creativecommons.org/licenses/by-nc-nd/4.0/>).

importance of appropriate tuning of the reduction and/or preparation procedures has been addressed to improve the catalysts' performance during anisole HDO.

## 1. Introduction

Accelerated consumption of fossil fuels has led to major global concerns with respect to availability and sustainability. The need for sustainable energy sources and corresponding conversion technologies is increasing for lowering the carbon footprint related to transportation and chemicals production. To address these concerns, out of several alternatives biomass appears to be a promising option to meet the growing sustainable energy demands. It is one of the most abundantly available renewable resources on earth and practically the only one to be converted to liquid fuel [1,2]. Lignocellulose is currently the most abundant source of plant biomass, which can be converted to bio-oil through catalytic and/or thermochemical processing (e.g., fast pyrolysis) [1]. Due to its high viscosity, high oxygen content, low heating value, pronounced thermal instability and incompatibility with conventional fuels, bio-oil tends to char surfaces and decrease efficiency [3]. Thus, bio-oil needs chemical upgrading to mitigate these issues related to the oxygen content, stability, viscosity, and energy value. Catalytic hydrodeoxygenation (HDO) of bio-oil seems to be an attractive route for improving the quality of the oil [4,5].

The complexity of lignin, and consequently of the derived fast pyrolysis oil, has prompted the use of model compounds such as phenolics, furans, ethers, acids etc. to study the intricacies of hydrodeoxygenation. Among the oxygenates in bio-oil, phenolics constitute one fourth fraction and are the most resistant to HDO [5,6]. Anisole, because of its methoxy group, has already been widely investigated as a model compound for lignin derived bio-oil [2,7–11]. It is desirable to break the  $C_{\text{aromatic}}\text{--O}$  bond in anisole rather than the  $C_{\text{aliphatic}}\text{--O}$  bond to eliminate the oxygen heteroatom, however, accomplishing that poses a specific challenge as the  $C_{\text{aromatic}}\text{--O}$  bond energy exceeds that of  $C_{\text{aliphatic}}\text{--O}$  by  $84\text{ kJ mol}^{-1}$  [5]. Moreover, deoxygenation is normally preferred over aromatic ring hydrogenation for minimizing the hydrogen consumption as well as to maintain appropriate aromatic content [12–14].

Catalytic HDO of bio-oils has been studied on noble metal catalysts such as Ru, Pt, Pd and also on traditional hydrotreating catalysts such as sulfided CoMo and NiMo [2,5,15,16]. Although sulfided catalysts exhibit superior activity in bio-oil HDO, due to low sulfur contents in bio-oil, additional sulfur need to be added to the feed to keep the catalysts active. Thus, leading to sulfur contamination of the end products. Noble metal catalysts are economically non-viable due to high hydrogen consumption and are susceptible to poisoning by low levels of contaminants such as iron or sulfur. Thus, significant challenges remain in the rational design of adequate HDO catalysts for bio-oil upgrading with lower  $\text{H}_2$  consumption, higher HDO activity, and longer catalyst life.

Preferably non-noble, non-sulfided HDO catalysts should be developed to overcome the issues mentioned above. Recently, major advances have been made in the area of transition metal based catalysts, particularly with respect to Mo oxide and carbide for HDO [9–11,17–20]. Previous reports have shown the significant potential of Mo based catalysts towards hydrogenolysis, hydrogenation and hydroisomerization type of reactions [21–27]. Román-Leshkov et al. demonstrated the  $\text{MoO}_3$  catalyst performance in cleaving  $C_{\text{aromatic}}\text{--O}$  bonds and highlighted the importance of  $\text{Mo}^{5+}$  species on the catalyst stability [9,10]. The latter species result from a partial carburization of the surface to transform  $\text{MoO}_3$  into an oxycarbonylhydride ( $\text{MoO}_x\text{C}_y\text{H}_z$ ) [10,22,28].  $\text{MoO}_3$  catalysts have also exhibited high alkane and/or aromatic yields (up to 90%) in the conversion of real bio-oil vapors [29]. An oxygen vacancy driven mechanism was hypothesized to be

responsible for HDO over both bulk and supported  $\text{MoO}_3$  catalysts [9,17]. Mortensen et al. discussed the oxidation of  $\text{Mo}_2\text{C}$  to  $\text{MoO}_2$  under HDO conditions, as a cause of catalyst deactivation [30]. Bhan and co-workers have shown that partially oxidized molybdenum carbide can selectively hydrodeoxygenate biomass-derived molecules with near absence of sequential hydrogenation [31,32]. The above studies indicate the critical role of intermediate state(s) between an oxide and a carbide form of Mo species on its catalytic performance, including stability. We have adopted a post-synthesis modification procedure on  $\text{MoO}_3$  using  $\text{H}_2/\text{CH}_4$  mixture, inspired by carburization procedures [33,34] to achieve the critical intermediate oxidation state of Mo oxide.

On supported  $\text{MoO}_3$  catalysts, interactions with the support lead to mixed oxide species. Generally, the mixed oxide concentrations vary with the Mo loading on the support and the calcination temperature, amongst others [35,36]. Moreover, structural changes of the mixed oxide as well the Mo oxide itself can affect the reducibility as well as catalyst activity [35–39]. The present work, hence, focuses on the development and characterization of supported molybdenum oxides with different Mo loadings and examines the impact of preparation conditions and catalyst surface composition on its activity and stability during catalytic HDO of anisole. Aiming at avoiding hydrothermal stability challenges of alumina supports [5], as well as to lower the potential for carbonaceous deposits formation, a less acidic surface, i.e.,  $\text{ZrO}_2$  was evaluated as support [40]. In addition, an insight into the anisole HDO reaction pathways is given through intrinsic kinetic experiments varying space-time, temperature, along with stability tests performed over present catalysts.

## 2. Experimental methods

### 2.1. Catalyst preparation

Molybdenum oxide catalysts supported on zirconia were prepared targeting three levels of Mo, determined by ICP-OES to be ca. 7, 12, and 19 wt%. An incipient wetness pore filling procedure was employed for impregnating the zirconia support with an aqueous solution of ammonium heptamolybdate ( $(\text{NH}_4)_6\text{Mo}_7\text{O}_{24}\cdot 4\text{H}_2\text{O}$ , Alfa Aesar). Zirconia (Alfa Aesar) pellets were first crushed and sieved to obtain the 100–300  $\mu\text{m}$  particle size fraction, which was subsequently calcined at 500  $^\circ\text{C}$  for 5 h prior to impregnation. After the impregnation, the samples were initially dried at room temperature for 12 h and afterwards at 110  $^\circ\text{C}$  for 24 h, followed by calcination under flowing air (ca. 150 ml/min) at 500  $^\circ\text{C}$  for 5 h. The calcined materials were referred as  $x\text{MoO}_3$  with “x” the Mo loading. Further, the calcined materials were subjected to a post-synthesis modification under  $\text{H}_2/\text{CH}_4$  gas mixture. The oxide sample was heated at a rate of 1  $^\circ\text{C min}^{-1}$  under  $\text{H}_2/\text{CH}_4$  (80% v/v) gas mixture till a target reduction temperature was reached and subsequently held there for 1 h at atmospheric conditions. As a part of this treatment, two different target temperatures, i.e., 550 and 700  $^\circ\text{C}$  were employed and the corresponding materials were referred as Mo550 and Mo700 respectively. This was followed by a passivation step with (1% v/v)  $\text{O}_2/\text{Ar}$  at room temperature for 2 h for subsequent transportation purposes of the catalyst.

### 2.2. Catalyst characterization

$\text{N}_2$  adsorption–desorption isotherms of the powdered catalyst samples were measured at  $-196\text{ }^\circ\text{C}$  using a Micromeritics TriStar II 3020 instrument. The specific surface area ( $S_{\text{BET}}$ ) was calculated by the Brunauer–Emmett–Teller (BET) method. Prior to these measurements,

the samples were outgassed at 200 °C for 2 h.

The total amount of Mo in as-prepared catalysts was determined by means of inductively coupled plasma optical emission spectroscopy (ICP-OES, ICAP 6500, Thermo Scientific). The samples were mineralized by alkaline fusion with Na-peroxide.

A Micromeritics AutoChem 2920 instrument with a thermal conductivity detector (TCD) was applied for the temperature programmed reduction, H<sub>2</sub>-TPR. Sample amounts of ca. 100 mg were loaded in a U-shaped tubular quartz reactor, with an internal thermocouple positioned at the level of the sample bed. To obtain the TPR profiles the temperature was progressively increased from ambient to 1000 °C at a rate of 10 °C/min in a mixture of 10 vol% H<sub>2</sub>/He (60 ml/min).

Ammonia temperature programmed desorption (NH<sub>3</sub>-TPD) experiments were conducted also on the AutoChem 2920 instrument. Prior to NH<sub>3</sub>-TPD, the sample was purged with high-purity (99.999%) helium (60 ml/min) at 200 °C for 1 h. After pretreatment, the sample was saturated with high purity anhydrous ammonia employing 4 vol% NH<sub>3</sub>/He (75 ml/min) at 80 °C for 2 h and subsequently flushed at 110 °C for 1 h to remove physisorbed ammonia. The TPD analysis was carried out from ambient temperature to 800 °C at a heating rate of 10 °C/min. The amount of NH<sub>3</sub> desorbed was quantified by calculating the area under the TPD curve.

The active surface adsorption properties were determined by volumetric CO chemisorption on a Micromeritics ASAP 2020 instrument. CO chemisorption provides a measure for the accessibility of the catalytically active phase, such as the Mo dispersion. The latter is obtained from the CO uptakes and the known molybdenum concentration in the samples, assuming a chemisorption stoichiometry of CO:Mo = 1:1. The catalyst (200 mg) was loaded in a U-shaped quartz reactor and initially evacuated at 120 °C for 60 min. Afterwards, it was reduced in flowing H<sub>2</sub> at 350 °C (heating rate 10 °C/min) with a hold time of 2 h in case of MoO<sub>3</sub> and 0.5 h in case of Mo550 and Mo700. Subsequently, it was evacuated at 350 °C for 50 min, then cooled down to 40 °C, and evacuated for another 30 min. The adsorption isotherms were measured at 40 °C by determining the adsorbed amount of CO at different pressures in the range 20–500 mmHg. Adsorbed volumes were obtained by extrapolating the linear part of the adsorption isotherm to zero pressure.

Raman spectroscopy of fresh catalyst samples in powder form was performed at room temperature with a RXN1 Raman spectrometer (Kaiser Optical Systems) equipped with a 532 nm Visible (VIS) solid-state diode pumped green laser operating at 40 mW using an optical probe. The collection optics system was used in the backscattering configuration.

X-ray Diffraction (XRD) patterns of the powdered catalyst samples were recorded at room temperature on a Siemens Diffractometer Kristalloflex D5000, using Cu K $\alpha$  radiation ( $\lambda = 1.54 \text{ \AA}$ ). The X-ray tube voltage was set to 40 kV and the current to 50 mA. XRD patterns were collected in the range of  $2\theta$  from 10° to 90° with a step size of 0.02°.

In-situ XRD measurements were performed in a reactor chamber housed inside a Bruker-AXS D8 Discover apparatus (Cu K $\alpha$  radiation of 1.54 Å). The reactor chamber had a Kapton foil window for X-ray transmission. The setup was equipped with a linear detector covering a range of 20° in  $2\theta$  with an angular resolution of 0.1°. The pattern acquisition time was 10 s. For each sample, approximately 20 mg of powdered sample was evenly spread on a single crystal Si wafer. Interaction of the catalyst material with the Si wafer was never observed. Before each experiment, the reactor chamber was evacuated to a base pressure of 4 Pa by a rotation pump. Gases were supplied to the reactor chamber from a rig with calibrated mass-flow meters. The evolution of the catalyst structure during TPR under H<sub>2</sub>/He and H<sub>2</sub>/CH<sub>4</sub> was investigated. A full XRD scan (15°–75° with step size of 0.02°) was taken at room temperature before and after TPR.

X-ray Photoelectron Spectroscopy (XPS) analysis was performed under ultrahigh vacuum conditions using an Axis Ultra DLD XP spectrometer from Kratos Analytical and monochromatic Al K $\alpha$  radiation ( $h\nu = 1486.6 \text{ eV}$ ). A pass energy of 160 eV was used for survey scans

and 20/40 eV was used for the individual core levels. Charge compensation using low energy electrons was applied during acquisition. The binding energy scales were calibrated to the adventitious carbon of C1s component at 284.6 eV. The background was subtracted using a Shirley function and the spectra were fitted using a convolution of Gaussian and Lorentzian functions.

Transmission Electron Microscopy (TEM) was used for structural analysis, while EDX yielded local elemental mapping. These techniques were implemented using a JEOL JEM-2200FS, Cs-corrected microscope operated at 200 kV, which was equipped with a Schottky-type field-emission gun, FEG, and EDX JEOL JED-2300D. All samples were deposited by immersion onto a lacey carbon film on a copper support grid.

The carbon content in spent and fresh catalyst materials was analyzed by CHNS elemental analysis. These measurements were performed on a Thermo Flash 2000 elemental analyzer using V<sub>2</sub>O<sub>5</sub> as catalyst. Sample cups are tightened and the analysis waiting time kept as short as possible to minimize re-adsorption of water, affecting the weight and elemental composition of the samples.

### 2.3. Catalyst testing

#### 2.3.1. Setup and operating conditions

Kinetic experiments for gas phase anisole HDO were carried out in a state of the art high throughput kinetic screening setup, HTK-S [41]. A schematic representation of the setup is provided in S.I. Fig. 1. The setup contains 16 parallel reactors, located in 4 blocks with 4 reactors each. A single feed to one reactor block is generated via 2 gas lines and 1 liquid line. Capillaries ensure an equal distribution of the total (gas and liquid) flow to the four reactors contained in a reactor block. In this work hydrogen diluted with helium was used as gas feed and anisole dissolved in n-hexane with some n-octane as an internal standard as the liquid feed. Both temperature and pressure are identical for all 4 reactors in a reactor block. The catalyst particles with mesh size 100–200  $\mu\text{m}$ , diluted with  $\alpha$ -alumina inert of the same size, were placed in the catalyst bed between two inert  $\alpha$ -alumina layers. The inert layer present on top of the catalyst bed aids the liquid feed vaporization and also ensures adequate mixing and development of a plug flow regime before reaching the catalyst bed. Filter frits are positioned at the reactor outlet to keep the bed in the desired position. The reactor outlet leads to a multiport valve, vent, and gas-liquid separator through a T-piece junction. This multiport valve allows selecting which reactor effluent will be sent to the GC for on-line analysis. In the present study, the downstream of the reactor outlet is heated up to 150 °C and diluted with N<sub>2</sub> to ensure that the effluent remains entirely in the vapor phase until it reaches the GC. The product stream is analyzed with the help of an on-line gas injection. The on-line analysis is performed with a DHA (Detailed Hydrocarbon Analyzer) TraceGC1310 equipped with 2 flame ionization detectors (FIDs, front and back). For the present analysis, the Front FID with a Rtx-PONA column (L = 100 m, i.d. = 0.25 mm) was used.

#### 2.3.2. Catalyst pre-treatment

Catalyst pre-treatment was carried out to transform the catalyst into its active form. The catalyst sample was dried at 180 °C first for 2 h under helium and subsequently heated till 350 °C at 5 °C min<sup>-1</sup> under H<sub>2</sub>/He (70% v/v) and maintained at that temperature for 1.5 h at a total pressure of 0.5 MPa. Calcined oxide materials (MoO<sub>3</sub>) were subjected to this pre-treatment. The performance of MoO<sub>3</sub> pretreated under H<sub>2</sub>/CH<sub>4</sub> (4 v/v) at 550 °C prior to the reaction, instead of the conventional H<sub>2</sub> reduction has also been verified and was found to result in a somewhat reduced activity, however, with a similar selectivity. As for the post-synthesis modified materials (Mo550 and Mo700), only the drying step under He was performed without the H<sub>2</sub> reduction step. After the pre-treatment, the temperature is changed to the target reaction temperature and, once stable, other operating parameters such as feed flow rates are set to start the actual kinetics measurement. The oxygen

passivation layer on Mo550 and M0700 is removed by H<sub>2</sub> at the reaction temperature, prior to feeding anisole.

### 2.3.3. Data treatment

The conversion of feed component *k*,  $X_k$ , is defined on a molar basis as shown in Eq. (1),

$$X_k = \frac{F_k^0 - F_k}{F_k^0} \quad (1)$$

$F_k^0$  and  $F_k$  represent the inlet and outlet molar flow rates of component *k*. The selectivity,  $S_{li}$ , for product *i* coming from the feed component *k* is calculated using Eq. (2) on an elemental carbon basis where  $cn_i$  is the number of carbon atoms in molecule *i*.

$$S_{li} = \frac{cn_i F_i}{cn_k (F_k^0 - F_k)} \quad (2)$$

$S_{HDO}$ ,  $Y_{HDO}$  are used to identify the hydrodeoxygenation performance of the investigated catalysts. The total amount of deoxygenated products formed on molar basis is defined as shown in Eqs. (3) and (4):

$$S_{HDO} = \frac{\sum F_{HDO}}{F_k^0 - F_k} \quad (3)$$

$$Y_{HDO} = \frac{\sum F_{HDO}}{F_k^0} \quad (4)$$

$F_{HDO}$  represents the total outlet molar flow rate of deoxygenated products coming from feed component *k*. The average turnover frequency (TOF, mol s<sup>-1</sup> mol<sub>Mo</sub><sup>-1</sup>) [42] was calculated from the difference in the inlet and outlet molar flow rates of components at 60 h time on stream (TOS) as shown in Eq. (5).

$$TOF_k = \frac{|(F_k^0 - F_k)|}{N_{Mo}} \quad (5)$$

$N_{Mo}$  represents the number of moles of exposed Mo atoms on the catalyst surface.  $N_{Mo}$  is calculated from the Mo dispersion obtained through CO chemisorption measurements.

### 2.3.4. Kinetic regime verification

Measurement of intrinsic kinetics requires that the performance is free from mass and heat transfer effects. Several criteria for the assessment of these effects have been proposed and successfully employed in the present work [43]. Mass transfer at the gas-solid interphase was assessed by calculating the dimensionless Carberry number,  $Ca$ , [44] at the extremes of the operating conditions. With Carberry numbers well below the limit value of 0.05, see also S.I. Table 1, such external mass transfer was found not to be limiting. The Weisz-Prater [45] criterion addresses the intra-particle diffusion for various reactants and products. At the present operating conditions, the Weisz modulus was well below the limit value of 0.08. The absence of heat transfer was verified via the criteria reported by Mears [46]. The temperature gradients were compared with the maximum allowed limits between the gas-solid interphase  $\Delta T_{G-S}$  and particle  $\Delta T_{int}$ . The most critical values of  $\Delta T_{G-S}$  and  $\Delta T_{int}$  were found to be at the highest operating temperature and are sufficiently lower than Mears' criterion of 2.2 °C, confirming the absence of heat transfer limitations. A tubular reactor is said to be operated in plug flow regime when the axial dispersion can be neglected [47] and uniformity in the radial direction is achieved [48]. It also requires a minimal pressure drop over the catalyst bed. The operating conditions for the anisole HDO experiments over the series of Mo catalysts are summarized in Table 1 and the assessment of the corresponding criteria for intrinsic kinetics [49] is given in S.I. Table 1.

## 3. Results and discussion

### 3.1. Material characterization

#### 3.1.1. Textural properties and elemental composition

BET measurements, see also Table 2 and S.I. Fig. 2, show that the specific surface area ( $S_{BET}$ ) of the catalysts decreases as a function of the Mo loading. Such a trend can be attributed to a gradually increased filling of the pore volume [50,51]. Post-synthesis modification under H<sub>2</sub>/CH<sub>4</sub> at 700 °C decreased  $S_{BET}$  of the investigated materials, an effect which became less pronounced with increasing Mo loading. This can be ascribed to the high temperature that favored the formation of relatively larger particles, predominantly at lower, i.e., 7 wt% Mo loading due to the amorphous form of Mo species present compared to more crystalline species present at 12 and 19 wt%. The less pronounced decrease in  $S_{BET}$  for 12Mo700 is at the limit of being significant while no clear difference was observed in case of 19 wt% loading, in agreement with the more pronounced crystallinity. The Mo surface densities per unit surface area (Mo atoms/nm<sup>2</sup>) were calculated from the MoO<sub>3</sub> concentration as determined by ICP and the BET surface area [39]. As can be seen from Table 2, Mo surface density increased with Mo loading.

S.I. Table 2 presents the CO chemisorption data over the investigated materials. It can be seen that the Mo dispersion values on all the catalysts are low. The evolution of the Mo species nature with increasing Mo loading and post-synthesis modification severity is further discussed via XPS and XRD analyses. The amount of exposed active Mo calculated through CO chemisorption data, see S.I. Table 2, was further used to assess the average turn over frequencies (TOF). Carbon analysis (S.I. Table 3) indicated that far less carbon remained on the oxide structure after the post-synthesis modification at 550 and 700 °C under H<sub>2</sub>/CH<sub>4</sub> mixture. This implies that the transformation occurring during this post-synthesis modification is essentially limited to MoO<sub>3</sub> reduction, possibly dominated by H<sub>2</sub> activation with a potential to create active defect sites induced by the treatment. The acidity of the investigated catalysts was quantified using the ammonia TPD method. The TPD profiles, see S.I. Fig. 9, present intense peaks only at low temperatures (150–270 °C) and weak peaks at higher temperatures (410–530 °C, 700–720 °C), implying the rather moderate acidity of the catalysts. The corresponding acidity values are given in S.I. Table 6.

#### 3.1.2. Crystallinity

Fig. 1 depicts the XRD patterns of the fresh supported Mo oxide catalysts. The diffractogram of the bare ZrO<sub>2</sub> support has also been included as a reference. As seen in Fig. 1, the characteristic peaks of Zr (MoO<sub>4</sub>)<sub>2</sub> are present only in the pattern corresponding to the high Mo-loaded sample, i.e., 19 wt%. Chen et al. [39] and El-sharkawy et al. [38] have reported that in the ZrO<sub>2</sub>-supported Mo oxide materials, an increase in Mo loading leads to higher Zr(MoO<sub>4</sub>)<sub>2</sub> concentrations with a more pronounced crystallinity. This observation explains the absence of peaks characteristic of crystalline Zr(MoO<sub>4</sub>)<sub>2</sub> on the lower, i.e., 7 and 12 wt%, Mo-loaded catalysts, see Fig. 1. Zr(MoO<sub>4</sub>)<sub>2</sub> may, however, still be present on both samples in XRD amorphous form, due to strong metal-support interactions (MSI). As can also be seen in Fig. 1, a MoO<sub>3</sub> phase is identified in both 12MoO<sub>3</sub> and 19MoO<sub>3</sub> samples, while

Table 1  
Performance test conditions.

Operating condition	Experimental range
Catalyst particle diameter (μm)	100–200
Temperature (°C)	300–360
Total pressure (MPa)	0.5
Space time (kg <sub>cat</sub> s mol <sub>anisole</sub> <sup>-1</sup> )	50–230
H <sub>2</sub> /anisole (mol <sub>H2</sub> mol <sub>anisole</sub> <sup>-1</sup> )	50

**Table 2**  
Catalyst and support properties.

Material	$S_{\text{BET}}$ ( $\text{m}^2/\text{g}$ )	Mo% (Mo/Zr)	Mo surface density (Mo/ $\text{nm}^2$ )	$\text{H}_2$ uptake ( $\mu\text{mol}/\text{g}$ )		
				Region I	Region II	Total
ZrO <sub>2</sub>	98.5 ± 0.9	–	–	–	–	–
7MoO <sub>3</sub>	91.6 ± 2.2	6.4 (0.1)	4.4	19.5	94.8	114.3
12MoO <sub>3</sub>	80.3 ± 2.2	11.2 (0.2)	8.8	66.6	120.2	186.8
19MoO <sub>3</sub>	53.4 ± 2.8	18.1 (0.36)	21.2	124.5	280.8	405.3

molybdena is XRD amorphous or highly dispersed form in the 7 wt% sample [38,40]. Crystallite sizes for MoO<sub>3</sub> and Zr(MoO<sub>4</sub>)<sub>2</sub> were calculated approximately equal to 100 and 60 nm respectively, in the case of 19MoO<sub>3</sub> sample, employing the Scherrer equation [52]. The above deductions from the XRD results were confirmed by Raman spectroscopy performed over the investigated supported Mo oxide materials, see Fig. 2. The Raman bands observed in the spectra of all three MoO<sub>3</sub> samples at 748, 945  $\text{cm}^{-1}$  indicate  $\nu_{\text{sym}}(\text{O}-\text{Mo}-\text{O})$  and  $\nu_{\text{asym}}(\text{O}-\text{Mo}-\text{O})$  vibrational modes of Zr(MoO<sub>4</sub>)<sub>2</sub> and the bands at 666, 819 and 996  $\text{cm}^{-1}$  indicate  $\nu_{\text{sym}}(\text{Mo}-\text{O}-\text{Mo})$ ,  $\nu_{\text{asym}}(\text{Mo}-\text{O}-\text{Mo})$ , and  $\nu(\text{Mo}=\text{O})$  vibrational modes of MoO<sub>3</sub> [36,53].

In-situ XRD analysis was also carried out to monitor the structural changes of the materials under a reducing atmosphere. Fig. 3 presents the XRD patterns of the 19MoO<sub>3</sub> sample after reduction using two types of treatments, i.e., under H<sub>2</sub>/He flow and under H<sub>2</sub>/CH<sub>4</sub> flow. Fig. 4(a, b) displays the time resolved in-situ XRD measurements during TPR under two different reducing conditions. Each yellow line segment designates the presence of a specific crystalline phase. The evolution of the crystalline species present in the sample is depicted as a function of reduction time, the latter determining the reduction temperature. The 2 $\theta$  angle window was chosen between 20 and 40° to capture the characteristic intense line segments of all possible species present in the sample. As can be seen in Fig. 4(a), the increase of the operating temperature under H<sub>2</sub>/He flow induces first the reduction of the Zr(MoO<sub>4</sub>)<sub>2</sub> around 400 °C followed by MoO<sub>3</sub> reduction to MoO<sub>2</sub>, in both

monoclinic (m) and hexagonal (h) phases. ZrO<sub>2</sub> phase is present in the sample throughout the investigated temperature window, while no line segment corresponding to (partially) reduced zirconium oxide species is spotted. The increase of the operating temperature under H<sub>2</sub>/CH<sub>4</sub> flow, up to 550 °C resulted in the virtually complete reduction of both Zr (MoO<sub>4</sub>)<sub>2</sub> and MoO<sub>3</sub> phases and the formation of monoclinic and hexagonal MoO<sub>2</sub>, as can be easily identified in Fig. 4(b). Further increase of the temperature up to 700 °C, seems to induce further conversion of monoclinic MoO<sub>2</sub>. However, no metallic nor carbide Mo phase was detected. It can, hence, be assumed that monoclinic MoO<sub>2</sub> is transformed into hexagonal MoO<sub>2</sub> under the investigated conditions [54,55].

### 3.1.3. Reduction behavior

Fig. 5 depicts the H<sub>2</sub>-TPR profiles of the supported Mo oxide samples. The TPR patterns suggest that the reduction of the supported molybdena occurs in two stages. The first is situated in the temperature range from 400 to 760 °C (region I), followed by a second one at temperatures exceeding 760 °C (region II) [40,56]. Within region I, the first peak around 416–438 °C can be attributed to the reduction of the mixed oxide phase Zr(MoO<sub>4</sub>)<sub>2</sub> and the second one around 479–535 °C to crystalline and/or octahedral MoO<sub>3</sub> by taking into account the ex-situ (Fig. 1) and in-situ (Fig. 4) XRD data analysis [37,40]. These two peaks shift to higher reduction temperatures with increasing Mo loading, which is attributed to the more pronounced crystallinity of the Zr (MoO<sub>4</sub>)<sub>2</sub> and MoO<sub>3</sub> phases, as depicted in Fig. 1 [57]. Within the region II, the peak around 832–913 °C is ascribed to the reduction of tetrahedral molybdena. This phase, the prevalent Mo oxide form at low Mo loadings is difficult to reduce due to strong metal-support interactions [37]. The further reduction of Mo<sup>4+</sup> species could also be associated with this high temperature peak, as observed on other supported-Mo materials [35,58]. The corresponding hydrogen uptake values, given in Table 2, were found to increase in a proportional manner with increasing Mo loading.

### 3.1.4. Surface composition

XPS spectra were acquired for the 12 wt% Mo oxide material (fresh and reduced) samples to investigate the surface composition as well as the nature of the surface Mo species. For this purpose, the high-

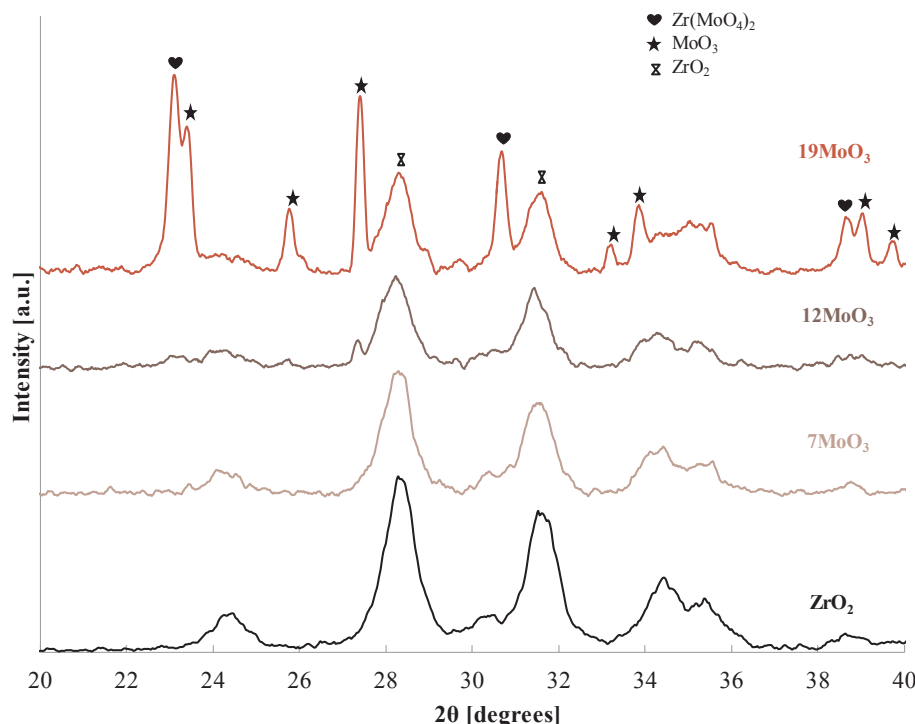


**Fig. 1.** X-ray diffractograms of zirconia support, 7MoO<sub>3</sub>, 12MoO<sub>3</sub>, 19MoO<sub>3</sub>, fresh samples.

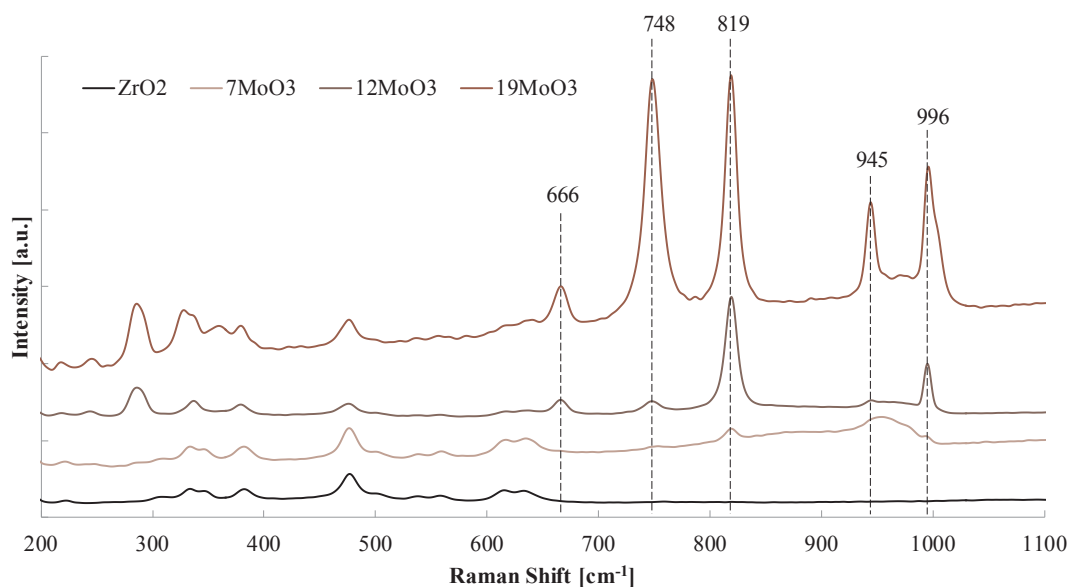


Fig. 2. Raman spectra of support  $ZrO_2$ ,  $7MoO_3$ ,  $12MoO_3$ , and  $19MoO_3$  fresh samples.

resolution XPS window of Mo 3d transitions was focused upon, see Fig. 6. The Mo 3d level consists of two spin orbit split contributions,  $3d_{5/2}$  and  $3d_{3/2}$ , separated by 3.2 eV, with an area, intensity ratio of 3:2 and identical full width at half maximum (FWHM). Mo  $3d_{5/2}$  and  $3d_{3/2}$  components are located at 232.55 and 235.7 eV respectively [59–61]. There seems to be a small shift towards higher binding energy, BE, compared to the BE value of Mo $3d_{5/2}$  in bulk  $MoO_3$  which is believed to

be caused by the metal-support interactions. FWHM of Mo $3d_{5/2}$  is in the range of 1.8–2.2, which is slightly higher compared to the FWHM of Mo $3d_{5/2}$  in bulk  $MoO_3$  [62,63]. This broadening can be attributed to various factors including (i) the presence of more than one type of Mo species with different chemical characteristics, and (ii) electron transfer between Mo and the support (metal-support interactions). Because of the use of an electron gun, differential charging stemming from poor

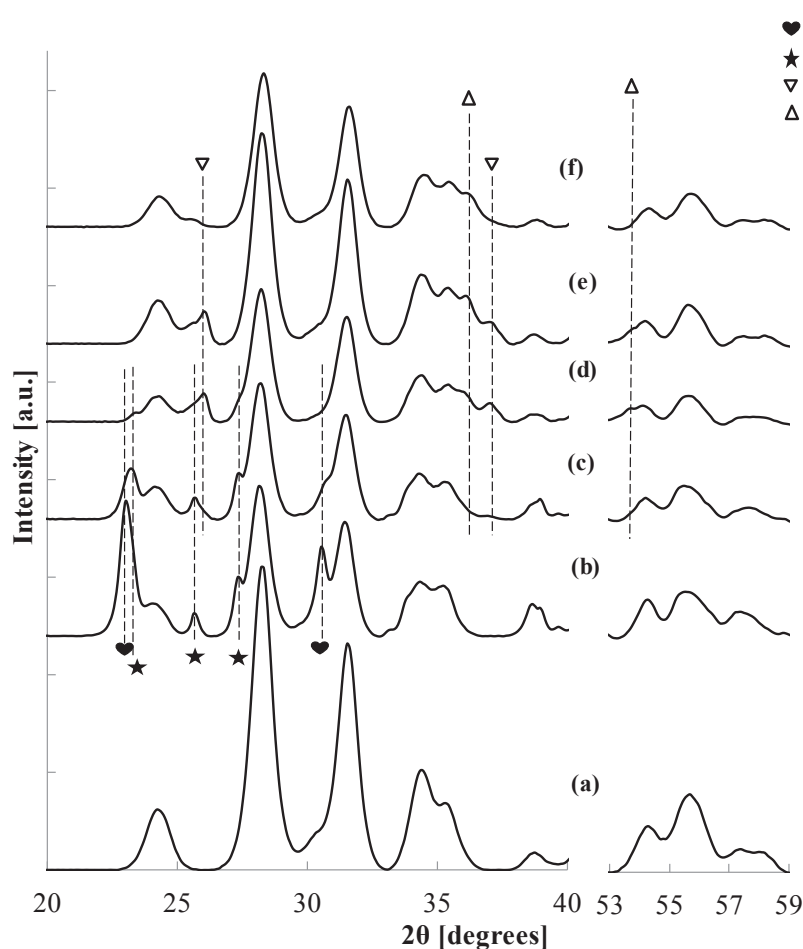


Fig. 3. XRD scans of support  $ZrO_2$  (a), fresh (b) and reduced (c, d, e, f)  $19MoO_3$  samples. (c) and (d) were obtained after reducing under  $H_2/He$  (10% v/v) mixture at 350 and 450 °C respectively. (e) and (f) were obtained after reducing under  $H_2-He-CH_4$  ( $H_2/CH_4 = 4$  v/v) mixture at 550 and 700 °C respectively.

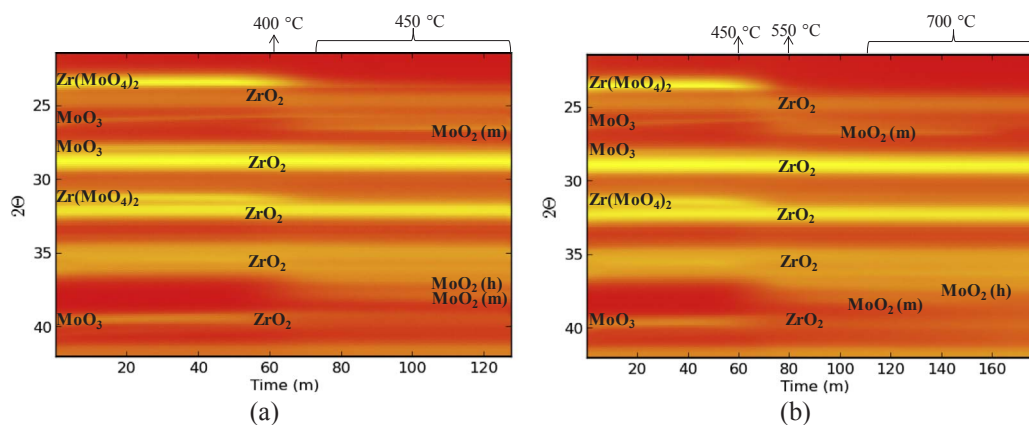


Fig. 4. Time resolved in-situ XRD for 19MoO<sub>3</sub> material during (a) TPR under H<sub>2</sub>/He (10% v/v) mixture; heating rate: 5 °C/min, maximum temperature 450 °C, hold time: 1 h. (b) TPR under H<sub>2</sub>-He-CH<sub>4</sub> (H<sub>2</sub>/CH<sub>4</sub> = 4 v/v) mixture; heating rate: 5 °C/min, maximum temperature 700 °C, hold time: 1 h. The X-axis follows the time scale according to the heating rate of the reduction, which started from ambient to the target (450 or 700 °C) value.

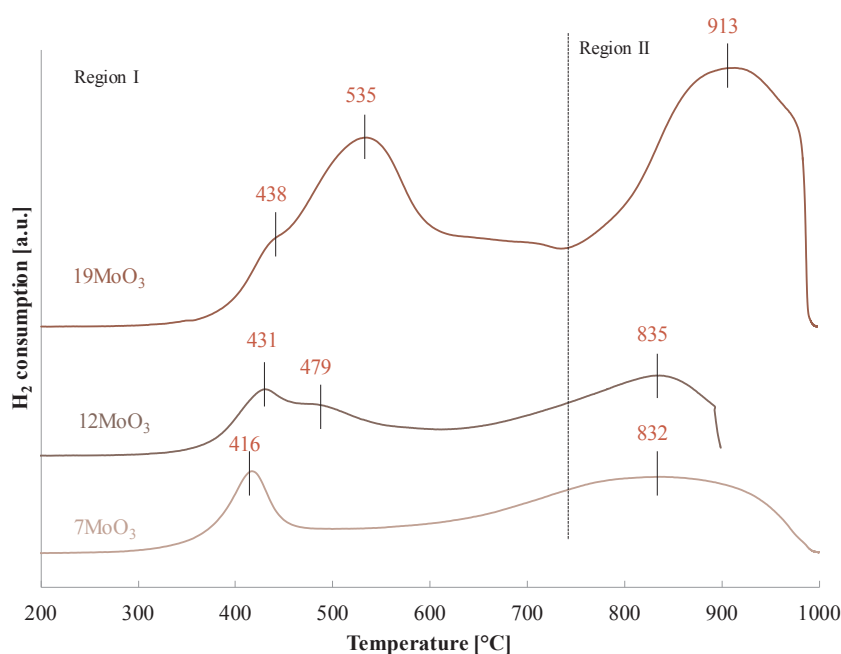


Fig. 5. H<sub>2</sub>-temperature programmed reduction (H<sub>2</sub>-TPR) of 7MoO<sub>3</sub>, 12MoO<sub>3</sub>, and 19MoO<sub>3</sub> samples.

conductivity of the samples could be discarded [62]. Prior to any deconvolution of the XPS data, it is already evident that all catalyst samples contain a significant fraction of Mo<sup>6+</sup> species in the form of MoO<sub>3</sub>.

After deconvolution of the XPS spectra, the contribution of the various Mo species such as Mo<sup>6+</sup>, Mo<sup>5+</sup>, Mo<sup>4+</sup> has been calculated, see Fig. 6. The fresh 12MoO<sub>3</sub> sample features only Mo<sup>6+</sup> species as shown in Fig. 6. A mild reduction of the 12MoO<sub>3</sub> sample at 350 °C, resulted in the presence of Mo<sup>5+</sup> species along with Mo<sup>6+</sup> species. In case of post-synthesis modification with H<sub>2</sub>/CH<sub>4</sub>, i.e., 12Mo550 and 12Mo700, peaks corresponding to Mo<sup>4+</sup> in addition to Mo<sup>5+</sup> surface species also appeared. The binding energies of Mo<sup>6+</sup>, Mo<sup>5+</sup>, Mo<sup>4+</sup> are found to be at 232.0–232.4, 231.0–231.6, and 229.1–229.7 respectively (S.I. Table 5), which is consistent with the reported values [61,64,65]. The prevalence of Mo<sup>5+</sup> species in reduced catalysts is indicative of the creation of active defects in the parent Mo oxide structure. It is reported that, in bulk MoO<sub>3</sub>, Mo<sup>5+</sup> species arise from either the transformation of MoO<sub>3</sub> to MoO<sub>x</sub>C<sub>y</sub>H<sub>z</sub> and/or the reduction of MoO<sub>3</sub> to MoO<sub>3-x</sub> [9,17,22]. Presence of metallic Mo has not been observed in any of the materials. The surface fraction of Mo with reduced valence states, especially Mo<sup>5+</sup> increases along with development of Mo<sup>4+</sup> in Mo550

and Mo770 compared to the mildly reduced MoO<sub>3</sub>, see Fig. 6. Although the intermediate state Mo<sup>5+</sup> was not observed through in-situ XRD measurements, its presence cannot be ruled out, as it may coexist in an amorphous form or in small crystallites. However, the reduction of MoO<sub>3</sub> (Mo<sup>6+</sup>) to MoO<sub>2</sub> (Mo<sup>4+</sup>) phase has been apparent through both XPS and XRD analyses.

### 3.1.5. Morphology and bulk composition

(S)TEM analysis along with EDX elemental mapping has been performed to determine the structural features of MoO<sub>3</sub> catalysts with increasing Mo loading. In case of 7MoO<sub>3</sub>, the particle size is difficult to estimate as molybdenum is homogeneously spread over the support zirconia making a contrast pattern between Mo and Zr quasi identical, which is illustrated by the EDX analysis, see Fig. 7(a). In case of 19MoO<sub>3</sub> there are more variations in the contrast between Mo and Zr elemental maps. This suggests coarse-scale inhomogeneity of Mo spread on the support surface of 19MoO<sub>3</sub> material, see Fig. 7(b), likely due to the formation of bigger MoO<sub>3</sub> crystals along with development of a mixed oxide, Zr(MoO<sub>4</sub>)<sub>2</sub>, which also has been evidenced through XRD. Moreover, EDX spectra of the samples (S.I. Fig. 5) were complicated to analyze due to a close overlap between characteristic Zr and Mo

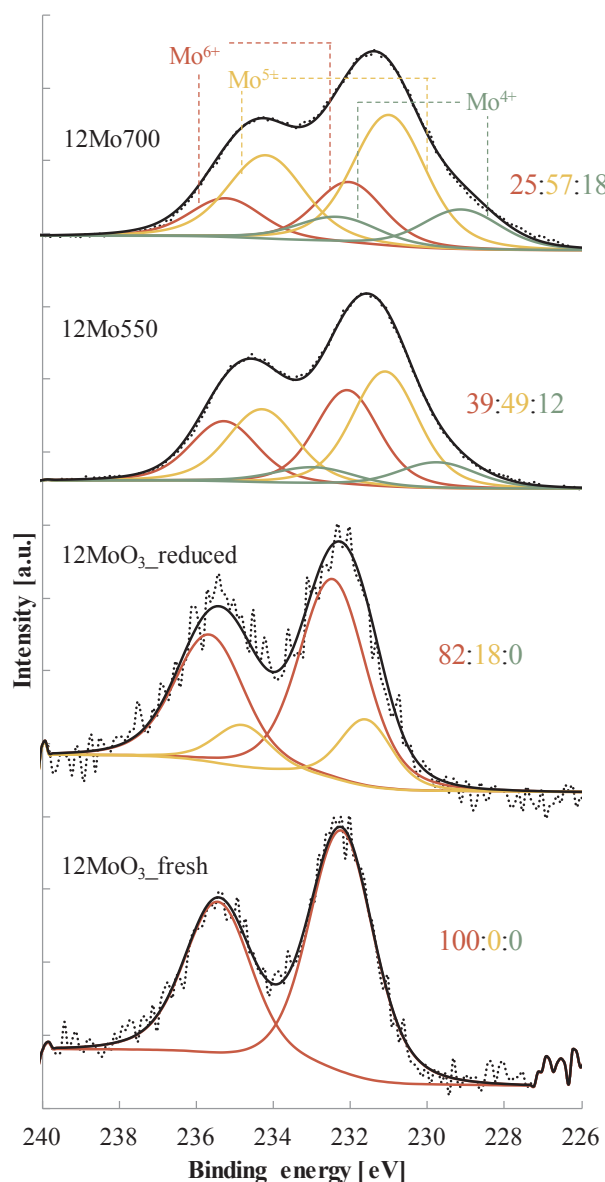


Fig. 6. High-resolution XPS of Mo 3d doublet transition of 12MoO<sub>3</sub> (fresh and reduced at 350 °C), 12Mo550, and 12Mo700 samples. A shorter measuring time was used to limit beam reduction for 12MoO<sub>3</sub> fresh and reduced samples.

analytical peaks. As it is difficult to estimate the particle size, for a quantitative understanding, the size of Mo oxide species aggregate is estimated from the HRTEM images, see Fig. 8. Aggregate sizes increased with the Mo loading from 7 to 19 wt%, and grew to a maximum size of approximately 150 nm in 19MoO<sub>3</sub>, see Fig. 8(b). At lower, i.e., 7 wt%, Mo loading, Mo aggregates are relatively small with their size not exceeding 20 nm, see Fig. 8(a). This is indeed in agreement with the already discussed concept that at lower Mo loading, Mo oxide species exists mainly as well-spread amorphous polymolybdates as well as Zr (MoO<sub>4</sub>)<sub>2</sub>, and at higher Mo loading as big size crystallites [37,51,58], which also has been observed through XRD results, see Fig. 1.

### 3.2. Catalytic performance

#### 3.2.1. Activity tests and reaction network elucidation

Catalyst performance was assessed using anisole HDO as a model reaction in a temperature range of 300–360 °C at 0.5 MPa total pressure, ensuring that the reaction was occurring in gas phase. The investigated catalysts were tested for their stability during anisole HDO at

340 °C and 0.5 MPa, employing a H<sub>2</sub> to anisole inlet ratio of 50 mol mol<sup>-1</sup> and a space time of 125 kg<sub>cat</sub> s mol<sub>anisole</sub><sup>-1</sup>. All MoO<sub>3</sub> catalysts exhibited a similar stability behavior with time on stream (TOS), i.e., the activity rapidly lines out during the first 20 h TOS and subsequently declines only moderately, see Fig. 9(a). Some activity decrease persisted up to 100 h TOS, though being relatively limited compared to the initial decrease. Mo550 and Mo700 exhibited a less pronounced initial lining out followed by a more stable behavior. Yet the initial conversions on Mo550 and Mo700 were lower in comparison to the MoO<sub>3</sub> catalysts, see Fig. 9(b) for the 12 wt% Mo catalysts. It indicates that the reduction treatment with H<sub>2</sub>/CH<sub>4</sub> enhances the catalyst stability under HDO conditions but decreases the overall activity, which is attributed to enrichment of Mo<sup>5+</sup> and Mo<sup>4+</sup> species respectively, see also section 3.2.2.

The products obtained were benzene, phenol, cresol, toluene, methyl anisole, and dimethyl phenol. Trace amounts of heavier aromatic products such as xylenes and trimethylbenzenes were also detected. Methane was the only light hydrocarbon by-product observed. The typical mass and carbon balances were closed within 100 ± 5%. Main product selectivities are plotted in Fig. 9(c, d). The deoxygenated product (benzene, toluene) selectivity exhibited a decreasing trend, just like the anisole conversion with the time on stream whereas the phenolic product (phenol, cresol, dimethyl phenol) selectivity increased. The presence of traces of xylenes and trimethylbenzenes implies further methylation of the aromatic ring. All investigated catalysts exhibited negligible selectivity towards aromatic ring hydrogenation in present range of operating conditions, except the formation of some traces of cyclohexene (< 1% selectivity). Hence, all catalysts exhibited high hydrogenolysis to hydrogenation ratio, see Table 3.

As can be seen in Table 3, there was no significant difference between the product selectivities over the investigated catalysts at an iso-conversion level of 40%. The performance of the catalysts investigated in the present work is in line with what has been reported for MoO<sub>3</sub> materials tested under similar HDO conditions [10].

Intrinsic kinetic data suggest that anisole transformation under present hydrotreating conditions occurs through a complex reaction network and that the investigated catalysts exhibit very high hydrogenolysis to hydrogenation ratio. To determine the reaction pathway, the evolution of product selectivities with space-time as well as temperature was investigated (S.I. Fig. 6). Also, the results from the catalyst stability experiments, i.e., the evolution of product selectivity with time on stream, see Fig. 9(c, d), contributed to this reaction mechanism elucidation. A reaction pathway that is consistent with the observations made on all catalysts is shown in Fig. 10. It is in line with earlier work reported in the literature for anisole HDO [66–72]. Anisole conversion at the present reaction conditions mainly proceeds via hydrogenolysis and methyl transfer reactions. The direct deoxygenation product, methanol, was not observed in the product stream at all conversion levels, suggesting that catalysts are more selective in cleaving C<sub>aliphatic</sub>–O bonds than C<sub>aromatic</sub>–O bonds in anisole [71,73]. This C<sub>aliphatic</sub>–O bond is indeed weaker than the C<sub>aromatic</sub>–O bond, i.e., the one connecting the methoxy group to the aromatic ring [5,74]. Initially, anisole is converted into phenol through demethylation by cleaving the C<sub>aliphatic</sub>–O bond followed by hydrogenolysis of the C<sub>aromatic</sub>–OH bond to produce benzene, which involves a partial hydrogenation of the phenolic ring near the C<sub>aromatic</sub>–OH bond, resulting in the temporary removal of the delocalization effect followed by rapid dehydration [25,69]. It results in the formation of benzene and water. Further, aromatic hydrogenation of benzene to cyclohexene was found to be very limited i.e., selectivity < 1% at the operating conditions used, and irrespective of the conversion levels. Fully hydrogenated products, i.e., methoxycyclohexane and cyclohexane were not observed at all. These results indicate that the present Mo catalysts possess an insignificant activity for aromatic ring hydrogenation, which is in agreement with prior HDO experimentation and, hence, can be considered as a typical feature of Mo based catalysts, in contrast with, e.g., Ni based ones

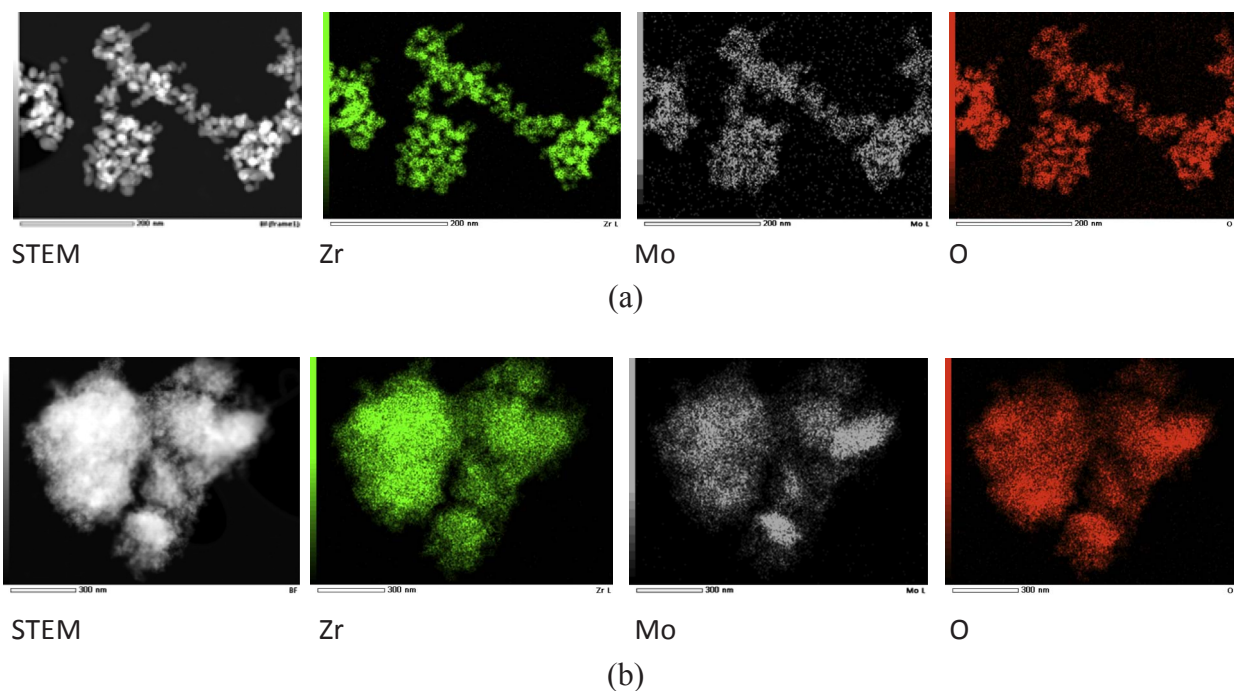


Fig. 7. STEM/EDX analysis of (a) 7MoO<sub>3</sub> (b) 19MoO<sub>3</sub> fresh samples.

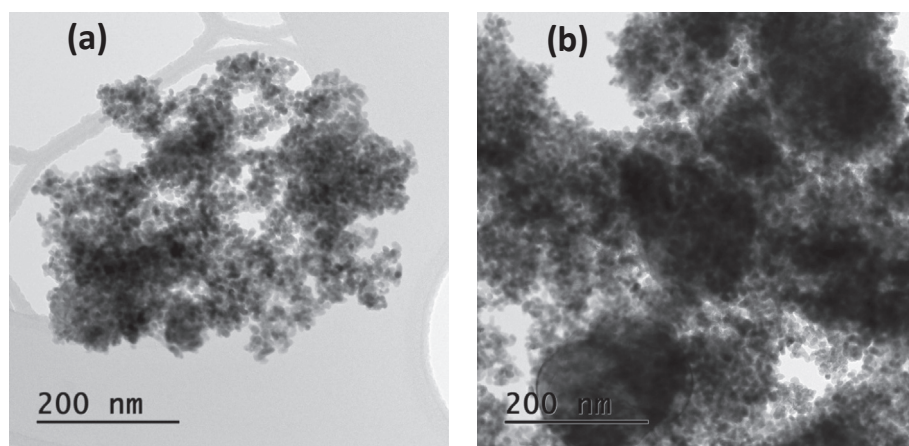


Fig. 8. HRTEM images of (a) 7MoO<sub>3</sub> and (b) 19MoO<sub>3</sub> fresh samples.

[9–11,17,20,72,75].

Another substantial route observed at the present operating conditions during the conversion of anisole is transalkylation. The ease of the Caliphatic–O bond cleavage and the moderate acidity of the catalysts promote methyl transfer reactions, i.e., demethylation of anisole and methylation onto the aromatic ring [76,77]. The produced data also imply the simultaneous occurrence of intermolecular and intramolecular methyl group transfers, e.g., formation of methyl anisole, cresol, and dimethyl phenol. Cresol further transforms into toluene through direct hydrogenolysis, see Fig. 9(d). In similar way, xylenes are formed from dimethyl phenol. Further aromatic ring methylation was also found to occur but only in trace amounts producing tri-methylated benzenes.

### 3.2.2. Catalyst activity-structure correlation

The activity of Mo catalysts is determined by the Mo dispersion as well as the nature of active sites. It is reported that for the formation of a monolayer on support surface, 0.16 wt% of MoO<sub>3</sub> is required per m<sup>2</sup>/g of the support [37,78]. The surface area of zirconia used for support amounts to 98.5 m<sup>2</sup>/g and, hence, the amount of MoO<sub>3</sub> required for monolayer coverage is 15.8 or 10.5 wt% of Mo. From the XRD data, it is

understood that as the Mo loading increases to 12 wt%, crystallites start to grow as the Mo coverage on the support surface reaches beyond mono layer capacity [40,57]. It has been reported that at lower Mo loadings, Mo-oxide exists as small patches of two-layer thickness on the support and upon reduction, coordinatively unsaturated sites will be created at the edges of these patches through oxygen removal [40,58,79]. Further increase in Mo loading leads to an increase in number of such patches, eventually covering the support surface to a monolayer level. Beyond which, the patches grow three dimensionally and result in crystallites thus decreasing the Mo dispersion. The present results can be explained with the help of the above concepts.

At 7 wt% Mo loading, MoO<sub>3</sub> and Zr(MoO<sub>4</sub>)<sub>2</sub> exist as amorphous polymolybdates and at 12 wt% small MoO<sub>3</sub> crystallites are present. As Mo loading reaches 19 wt%, intense crystalline MoO<sub>3</sub> peaks emerge along with mixed oxide Zr(MoO<sub>4</sub>)<sub>2</sub> crystal peaks, see Fig. 1. The intermediate Mo level loaded catalyst, i.e. 12MoO<sub>3</sub>, exhibited the highest activity per catalyst mass, see Fig. 11(a). This can be explained by the relatively higher amounts of exposed Mo on the catalyst surface at 12% Mo loading compared to other two Mo loadings and, hence, a maximum availability of active sites on this catalyst [35], see S.I. Table 2. It is understood from H<sub>2</sub>-TPR measurements that the total amount of

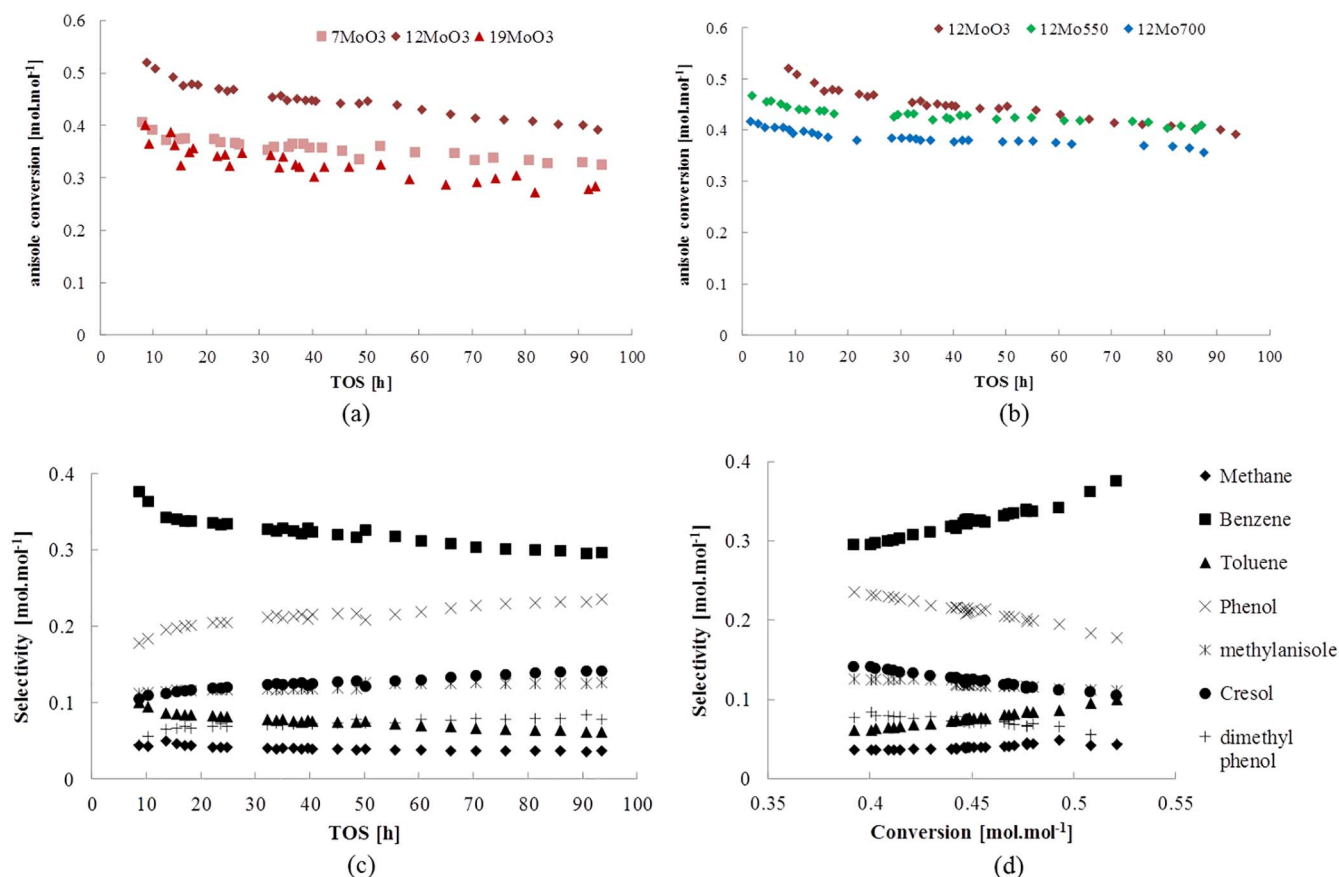


Fig. 9. Stability tests of (a) Mo oxide catalysts. (b) 12MoO<sub>3</sub>, 12Mo550 and 12Mo700 (c) Main product selectivity with TOS for the 12MoO<sub>3</sub> catalyst. (d) Main product selectivity vs. anisole conversion during TOS experiment with 12MoO<sub>3</sub> catalyst. Operating conditions: T = 340 °C, P<sub>T</sub> = 0.5 MPa, H<sub>2</sub>/anisole = 50 mol mol<sup>-1</sup>, W/F<sup>0</sup> = 125 kg<sub>cat</sub> s mol<sub>anisole</sub><sup>-1</sup>.

Table 3

Product selectivity (%) during anisole HDO (T = 340 °C, P = 0.5 MPa, H<sub>2</sub>/anisole = 50 mol mol<sup>-1</sup>, space time = 125–230 kg s mol<sup>-1</sup>) over MoO<sub>3</sub>, Mo550, and Mo700 catalysts at iso-conversion (≈ 40%).

	7MoO <sub>3</sub>	12MoO <sub>3</sub>	12Mo550	12Mo700	19MoO <sub>3</sub>
<i>Cyclic hydrocarbons (deoxygenated products)</i>					
Benzene	28.9	29.6	30.6	34.4	29.1
Toluene	8.5	6.2	6	8	7.9
Di & Tri methyl benzenes	2.2	2.1	2.5	3.4	2
Cyclohexene	0.3	0.5	0.3	0.2	0.4
S <sub>HDO</sub>	39.9	38.4	39.4	46	39.4
<i>Light hydrocarbons</i>					
Methane	2.9	3.6	3.9	4.5	3.5
<i>Oxygenates</i>					
Phenol	21.8	23.5	22.9	20.2	21.5
Cresol	14.9	14.1	14.4	12.1	14.8
Methyl anisole	10.7	12.6	11.2	10.5	10.9
Di methyl phenols	9.8	7.8	8.2	6.7	9.9

reducible Mo species increases with the Mo loading, see Table 2, however, relative to the total Mo amount a maximum number of active sites is available on 12MoO<sub>3</sub> at the tested operating conditions for anisole HDO, even resulting in higher anisole conversions. On the catalyst with 19 wt% Mo loading, the development of MoO<sub>3</sub> and mixed oxide, Zr(MoO<sub>4</sub>)<sub>2</sub>, crystals results in a reduced availability of active Mo sites. It has been reported that the activity of MoO<sub>3</sub> catalysts originates from the creation of oxygen vacancies (i.e., MoO<sub>3-x</sub>) through catalyst pre-treatment [9,80,81]. Moreover, oxygen vacancy creation capacity is closely related to the hydrodeoxygenation ability in similar catalysts [19]. It is understood from in-situ XRD measurements (Fig. 4 and S.I. Fig. 4) that Zr(MoO<sub>4</sub>)<sub>2</sub> is more easily reducible than MoO<sub>3</sub>. The

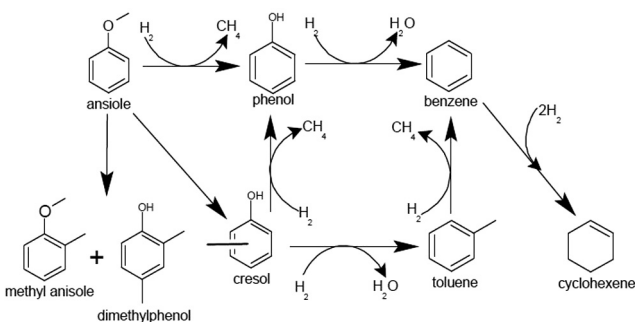


Fig. 10. Proposed anisole HDO reaction pathways.

adequate reducibility of the mixed oxide, Zr(MoO<sub>4</sub>)<sub>2</sub>, as well as MoO<sub>3</sub> to create necessary oxygen vacancies is critical in improving the overall catalyst performance. Activity per catalyst mass is proportional to the number of Mo sites calculated through CO chemisorption. The activity trend with Mo loading is similar at all three investigated temperature levels, see Fig. 11(a). At higher temperatures, the difference in anisole conversion is much more pronounced than at lower temperatures.

As can be seen in Fig. 11(b), 12MoO<sub>3</sub> produced the highest yield in HDO (Y<sub>HDO</sub>) products amongst the oxide catalysts, which is attributed to the corresponding high conversion of anisole over this catalyst, see Fig. 11(a). To determine the TOF over the above catalysts, their activity is normalized to the amount of active sites calculated through CO chemisorption.

As seen in Fig. 12(a) and S.I. Fig. 7(a), 7MoO<sub>3</sub> exhibited a higher TOF<sub>anisole</sub> and product yield per site compared to higher Mo loaded (i.e., 12 and 19%) catalysts. The comparison of the activity per catalyst mass with TOF indicates that the number of active sites increases with

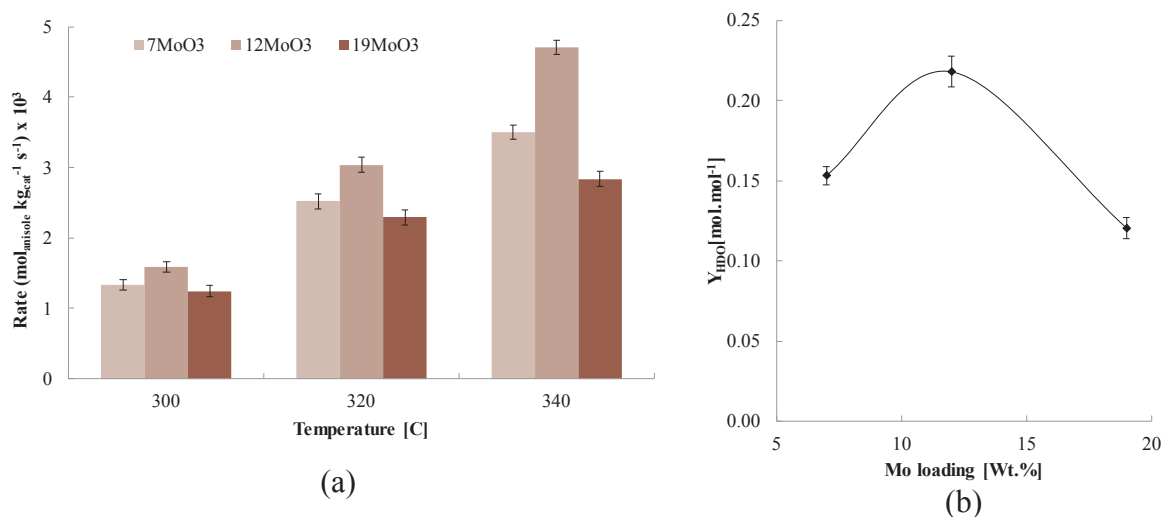


Fig. 11. Reaction rate per kilogram of catalyst of (a) Mo oxides at various reaction temperatures and (b) the deoxygenation yield ( $Y_{\text{HDO}}$ ) of Mo oxides at 340 °C. Other operating conditions:  $P_{\text{T}} = 0.5$  MPa,  $\text{H}_2/\text{anisole} = 50$  mol mol<sup>-1</sup>,  $W/F^* = 125$  kg<sub>cat.</sub> s mol<sub>anisole</sub><sup>-1</sup>. TOS = 40 h.

Mo loading and reaches a maximum at 12 wt% Mo (S.I. Table 2) and along with the Mo loading, the collective nature of active sites changes as well as the corresponding MoO<sub>3</sub>-ZrO<sub>2</sub> interactions in the case of the oxide catalysts. For the presently investigated catalysts, it has indeed been observed through H<sub>2</sub>-TPR and in-situ XRD measurements that reduction of both Zr(MoO<sub>4</sub>)<sub>2</sub> and MoO<sub>3</sub> results in the creation of active Mo, see Figs. 4 and 5. At low Mo loading, i.e., in case of 7MoO<sub>3</sub>, the active form of the catalyst is most likely obtained from the reduction of mainly the amorphous Zr(MoO<sub>4</sub>)<sub>2</sub> and partly from the reduction of polymolybdates. It could be deduced that the reduction of Zr(MoO<sub>4</sub>)<sub>2</sub> results in relatively higher active Mo compared to the reduction of MoO<sub>3</sub>. In contrast, the development of crystalline Zr(MoO<sub>4</sub>)<sub>2</sub> as well as MoO<sub>3</sub> in case of 12MoO<sub>3</sub> and 19MoO<sub>3</sub> inhibits the necessary Mo oxide reduction.

Mo550 and Mo700 displayed high TOF values compared to their oxide analogues, see Fig. 12(b), S.I. Fig. 7(b). It is understood from XPS analysis of the materials that, through post-synthesis modification, most of MoO<sub>3</sub> is converted from Mo<sup>6+</sup> state to reduced oxide states (Mo<sup>5+</sup> and Mo<sup>4+</sup>) on the catalyst surface. The pronounced concentration of such reduced Mo form (Mo<sup>5+</sup>), see Fig. 6, indicates that it is the main active phase accounting for the catalyst activity. Moreover, increased

Mo<sup>5+</sup> concentration in Mo550 and Mo700, improved catalyst stability with TOS, see Fig. 9(b), indicative of stable active phase. Mo<sup>5+</sup> has been reported to account for the catalyst activity during oxygenate HDO with Mo<sup>4+</sup> being relatively less active [10,82]. Although XRD indicated the presence of crystalline MoO<sub>2</sub> in Mo550 and Mo700, see S.I. Fig. 3, the subsequent activity tests showed that the modification under H<sub>2</sub>/CH<sub>4</sub> enhanced the turnover frequency (TOF), see Fig. 12(b). This is due to the generation of defects induced by the post-synthesis modification along with MoO<sub>3</sub> reduction to MoO<sub>2</sub> species [22,28]. Prasomsri et al. [10] reported that during oxygenate HDO, the nature of active sites transforms dynamically with the oxygenate stream and the most active form of the Mo species is an intermediate Mo phase (MoO<sub>x</sub>C<sub>y</sub>H<sub>z</sub>) associated with oxygen, carbon and hydrogen. In the present case, it is most likely that the most active intermediate Mo state has already been created through post-synthesis treatment under H<sub>2</sub>/CH<sub>4</sub> of precursor oxide (MoO<sub>3</sub>) prior to the anisole HDO reaction, as indicated by the increase in Mo<sup>5+</sup> concentration, see Fig. 6. In the case of MoO<sub>3</sub> catalysts, presence of rather lower Mo<sup>5+</sup> concentration during anisole HDO resulted in relatively lower TOF compared to Mo550 and Mo700 [17]. No change in TOF has been observed between Mo550 and Mo700. Increase in treatment temperature from 550 to 700 °C

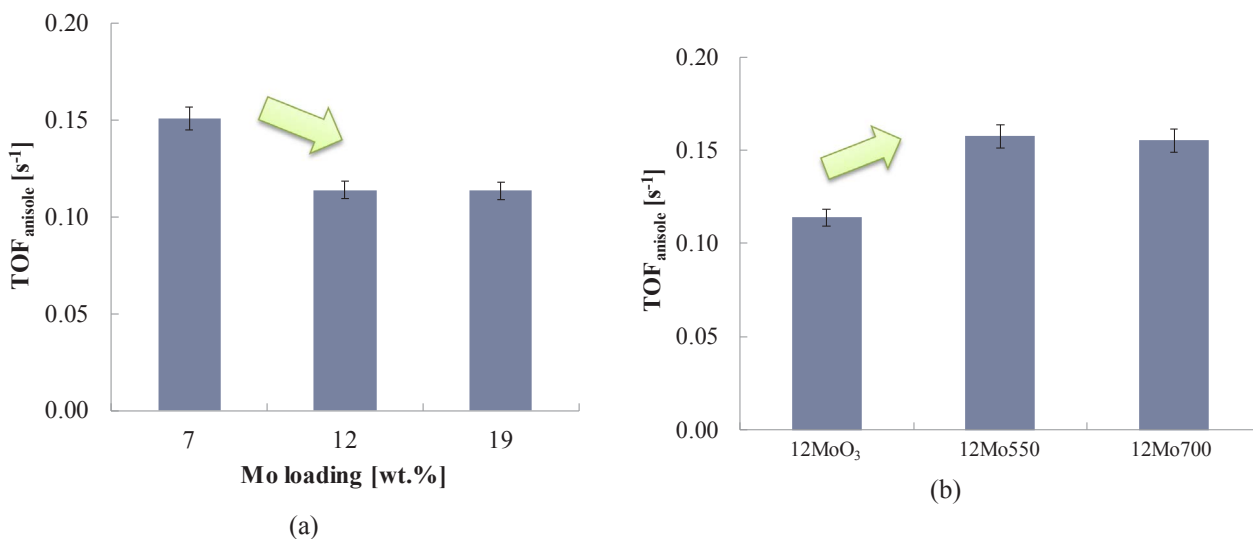


Fig. 12. TOF<sub>anisole</sub> of (a) oxide catalysts with varying Mo loading, (b) 12MoO<sub>3</sub>, 12Mo550, and 12Mo700. Operating conditions:  $T = 340$  °C,  $P_{\text{T}} = 0.5$  MPa,  $\text{H}_2/\text{anisole} = 50$  mol mol<sup>-1</sup>,  $W/F^* = 125$  kg<sub>cat.</sub> s mol<sub>anisole</sub><sup>-1</sup>.

decreased the anisole conversion but retained relatively same TOF. An adequately reduced and stable Mo state is the target property for present Mo catalyst material under oxygenate HDO reaction conditions [10,17]. As shown in Fig. 9(b), the total conversion decreases with the post-synthesis modification, yet the TOF increases, see Fig. 12(b), which is attributed to the development of defects in the Mo oxide structure due to treatment under H<sub>2</sub>/CH<sub>4</sub>. It is reported that an increase in Mo<sup>4+</sup> concentration decreases the overall activity of Mo catalysts for oxygenate HDO [10,30]. The decrease in activity displayed in Fig. 9(b), see also section 3.2.1, among different 12 wt% Mo catalysts can be attributed to the increase in Mo<sup>4+</sup>, which has also been observed through XRD (S.I. Fig. 3(a)) and XPS (Fig. 6) analyses of Mo550 and Mo700 catalysts. The differences in catalytic performance between monoclinic and hexagonal MoO<sub>2</sub> are considered negligible in view of the low activity of MoO<sub>2</sub>. The low overall activity exhibited by 12Mo700 in comparison to 12Mo550 is attributed to the presence of a higher amount of Mo<sup>4+</sup> or MoO<sub>2</sub> present. Hence, it can be deduced that the creation of strong Mo active sites for an oxygenate HDO highly depends on appropriate tuning of H<sub>2</sub> pre-treatment coupled with post-synthesis modifications for the catalysts. The evolution of surface composition, catalytic functionality in an oxygenate environment presents unique challenges in studying the structural and chemical changes of these materials and highlights the critical importance of an in-situ catalyst transformation study in assessing the active site requirements in these materials for bio-oil HDO.

The morphology of the catalyst materials is intact even after 100 h on stream. No evidence of sintering is identified, see S.I. Fig. 8. Increase in carbon content was observed on catalysts after 100 h TOS under anisole HDO conditions, see S.I. Table 3 and S.I. Table 4. The excess carbon could suggest poly-condensation of oxygenate feed and/or product on the catalyst surface, covering the active sites. This could be a reason for the initial decrease in anisole conversion.

#### 4. Conclusions

A series of ZrO<sub>2</sub> supported Mo oxide catalysts were prepared and characterized by a wide range of physicochemical techniques and their catalytic activity was evaluated using anisole hydrodeoxygenation as a model reaction. While MoO<sub>3</sub> and Zr(MoO<sub>4</sub>)<sub>2</sub> species were found to be amorphous in the 7 wt% Mo loaded material(s), their crystallinity increased significantly with Mo loading up to 19 wt%. A H<sub>2</sub>/CH<sub>4</sub> (80/20 vol%) treatment essentially transformed MoO<sub>3</sub> into a material with increased amounts of lower Mo oxidation state(s) such as Mo<sup>5+</sup> and Mo<sup>4+</sup>, as could be derived from XPS and (in-situ) XRD analyses. The catalyst activity for anisole HDO was closely related to the availability of active Mo oxide defects, i.e., Mo<sup>5+</sup> species. The catalyst with 12 wt% Mo loading exhibited the highest anisole conversion amongst the investigated catalysts. The highest TOF<sub>anisole</sub> (0.15 s<sup>-1</sup>) was observed over the 7 wt% Mo catalyst(s). Mo550 and Mo700 showed relatively higher stability as well as TOF compared to MoO<sub>3</sub> catalysts. Hydrodeoxygenation only occurred as a secondary reaction preceded by methyl transfer reactions yielding phenol and cresol. Aromatic hydrogenation was limited in the investigated range of operating conditions, also indicative of low hydrogen consumption. Product selectivity was found not to be affected by the deployed Mo loading and catalyst preparation conditions. Overall, the investigated materials exhibited up to 50% selectivity towards hydrodeoxygenation during anisole HDO with an adequate stability making them potential alternatives for metal sulfide and noble metal catalysts.

#### Acknowledgments

This work is supported by the Innovative Catalyst Design for large-scale sustainable processes (i-CaD) project, which is an ERC consolidator grant, by the European Commission in the 7th Framework Programme (GA no 615456). It also fits in the framework of the FAST

industrialization by Catalyst Research and Development (FASTCARD) project, which is a large scale collaborative project supported by European Commission in the 7th Framework Programme (GA no 604277).

#### Appendix A. Supplementary data

Supplementary data associated with this article can be found, in the online version, at <http://dx.doi.org/10.1016/j.cej.2017.10.090>.

#### References

- [1] J.C. Serrano-Ruiz, J.A. Dumesic, Catalytic routes for the conversion of biomass into liquid hydrocarbon transportation fuels, *Energy Environ. Sci.* 4 (2011) 83–99.
- [2] G.W. Huber, S. Iborra, A. Corma, Synthesis of transportation fuels from biomass: chemistry, catalysts, and engineering, *Chem. Rev.* 106 (2006) 4044–4098.
- [3] D.C. Elliott, Historical developments in hydroprocessing bio-oils, *Energy Fuels* 21 (2007) 1792–1815.
- [4] C.J. Zhang Qi, Wang Tiejun, Xu Ying, Review of biomass pyrolysis oil properties and upgrading research, *Energy Convers. Manage.* 48 (2007) 87–92.
- [5] E. Furimsky, Catalytic hydrodeoxygenation, *Appl. Catal. A: General* 199 (2000) 147–190.
- [6] P.C.A.B. Joseph Zakzeski, Anna L. Jongorius, Bert M. Weckhuysen, The catalytic valorization of lignin for the production of renewable chemicals, *Chem. Rev.* 110 (2010) 3552–3599.
- [7] S. Jin, Z. Xiao, C. Li, X. Chen, L. Wang, J. Xing, W. Li, C. Liang, Catalytic hydrodeoxygenation of anisole as lignin model compound over supported nickel catalysts, *Catal. Today* 234 (2014) 125–132.
- [8] X. Zhang, X. Chen, S. Jin, Z. Peng, C. Liang, Ni/Al<sub>2</sub>O<sub>3</sub> catalysts derived from layered double hydroxide and their applications in hydrodeoxygenation of anisole, *ChemistrySelect* 1 (2016) 577–584.
- [9] T. Prasomsri, T. Nimmanwudipong, Y. Román-Leshkov, Effective hydrodeoxygenation of biomass-derived oxygenates into unsaturated hydrocarbons by MoO<sub>3</sub> using low H<sub>2</sub> pressures, *Energy Environ. Sci.* 6 (2013) 1732–1738.
- [10] T. Prasomsri, M. Shetty, K. Murugappan, Y. Román-Leshkov, Insights into the catalytic activity and surface modification of MoO<sub>3</sub> during the hydrodeoxygenation of lignin-derived model compounds into aromatic hydrocarbons under low hydrogen pressures, *Energy Environ. Sci.* 7 (2014) 2660–2669.
- [11] W.-S. Lee, Z. Wang, R.J. Wu, A. Bhan, Selective vapor-phase hydrodeoxygenation of anisole to benzene on molybdenum carbide catalysts, *J. Catal.* 319 (2014) 44–53.
- [12] J.M. Huamin Wang, Yong Wang, Recent advances in hydrotreating of pyrolysis bio-oil and its oxygen-containing model compounds, *ACS Catal.* 3 (2013) 1047–1070.
- [13] S. Jin, Z. Xiao, X. Chen, L. Wang, J. Guo, M. Zhang, C. Liang, Cleavage of lignin-derived 4-O-5 aryl ethers over nickel nanoparticles supported on niobic acid-activated carbon composites, *Ind. Eng. Chem. Res.* 54 (2015) 2302–2310.
- [14] S. Jin, X. Chen, C. Li, C.W. Tsang, G. Lafaye, C. Liang, Hydrodeoxygenation of lignin-derived diaryl ethers to aromatics and alkanes using nickel on Zr-doped niobium phosphate, *ChemistrySelect* 1 (2016) 4949–4956.
- [15] A. Gutierrez, R.K. Kaila, M.L. Honkela, R. Slioor, A.O.I. Krause, Hydrodeoxygenation of guaiacol on noble metal catalysts, *Catal. Today* 147 (2009) 239–246.
- [16] B. Guvenatam, O. Kursun, E.H.J. Heeres, E.A. Pidko, E.J.M. Hensen, Hydrodeoxygenation of mono- and dimeric lignin model compounds on noble metal catalysts, *Catal. Today* 233 (2014) 83–91.
- [17] M. Shetty, K. Murugappan, T. Prasomsri, W.H. Green, Y. Román-Leshkov, Reactivity and stability investigation of supported molybdenum oxide catalysts for the hydrodeoxygenation (HDO) of m-cresol, *J. Catal.* 331 (2015) 86–97.
- [18] S.A.W. Hollak, R.W. Gosselink, D.S. van Es, J.H. Bitter, Comparison of tungsten and molybdenum carbide catalysts for the hydrodeoxygenation of oleic acid, *ACS Catal.* 3 (2013) 2837–2844.
- [19] T.J. Thibodeau, A.S. Canney, W.J. DeSisto, M.C. Wheeler, F.G. Amar, B.G. Frederick, Composition of tungsten oxide bronzes active for hydrodeoxygenation, *Appl. Catal. A: General* 388 (2010) 86–95.
- [20] W.-S. Lee, Z. Wang, W. Zheng, D.G. Vlachos, A. Bhan, Vapor phase hydrodeoxygenation of furfural to 2-methylfuran on molybdenum carbide catalysts, *Catal. Sci. Technol.* 4 (2014) 2340–2352.
- [21] M.J. Ledoux, P. Del Gallo, C. Pham-Huu, A.P. York, Molybdenum oxycarbide isomerization catalysts for cleaner fuel production, *Catal. Today* 27 (1996) 145–150.
- [22] C. Bouchy, C. Pham-Huu, B. Heinrich, C. Chaumont, M.J. Ledoux, Microstructure and characterization of a highly selective catalyst for the isomerization of alkanes: a molybdenum oxycarbide, *J. Catal.* 190 (2000) 92–103.
- [23] A. Goguet, S. Shekhtman, F. Cavallaro, C. Hardacre, F. Meunier, Effect of the carburization of MoO<sub>3</sub>-based catalysts on the activity for butane hydroisomerization, *Appl. Catal. A: General* 344 (2008) 30–35.
- [24] V.M.L. Whiffen, K.J. Smith, Hydrodeoxygenation of 4-methylphenol over unsupported MoP, MoS<sub>2</sub>, and MoO<sub>3</sub> catalysts, *Energy Fuels* 24 (2010) 4728–4737.
- [25] F. Massoth, P. Politzer, M. Concha, J. Murray, J. Jakowski, J. Simons, Catalytic hydrodeoxygenation of methyl-substituted phenols: correlations of kinetic parameters with molecular properties, *J. Phys. Chem. B* 110 (2006) 14283–14291.
- [26] J.S. Lee, S. Locatelli, S. Oyama, M. Boudart, Molybdenum carbide catalysts 3. Turnover rates for the hydrogenolysis of n-butane, *J. Catal.* 125 (1990) 157–170.
- [27] B. Dhandapani, T. St Clair, S.T. Oyama, Simultaneous hydrodesulfurization,

- hydrodeoxygenation, and hydrogenation with molybdenum carbide, *Appl. Catal. A- General* 168 (1998) 219–228.
- [28] Pascale Delporte, Frederic Meunier, Cuong Pham-Huu, Philippe Venneque, Marc J. Ledoux, J. Guille, Physical characterization of molybdenum oxycarbide catalyst; TEM, XRD and XPS, *Catal. Today* 23 (1995) 251–267.
- [29] M.W. Nolte, J. Zhang, B.H. Shanks, Ex situ hydrodeoxygenation in biomass pyrolysis using molybdenum oxide and low pressure hydrogen, *Green Chem.* 18 (2016) 134–138.
- [30] P.M. Mortensen, H.W. de Carvalho, J.-D. Grunwaldt, P.A. Jensen, A.D. Jensen, Activity and stability of Mo<sub>2</sub>C/ZrO<sub>2</sub> as catalyst for hydrodeoxygenation of mixtures of phenol and 1-octanol, *J. Catal.* 328 (2015) 208–215.
- [31] M.M. Sullivan, C.-J. Chen, A. Bhan, Catalytic deoxygenation on transition metal carbide catalysts, *Catal. Sci. Technol.* 6 (2016) 602–616.
- [32] M.M. Sullivan, A. Bhan, Acetone hydrodeoxygenation over bifunctional metallic-acidic molybdenum carbide catalysts, *ACS Catal.* 6 (2016) 1145–1152.
- [33] M. Boudart, S. Oyama, L. Leclercq, Molybdenum carbide oxycarbide and nitride as catalysts in the activation of CO, NN, CC and HH bonds, *Stud. Surf. Sci. Catal.* 7 (1981) 578–590.
- [34] S.T. Oyama, Preparation and catalytic properties of transition-metal carbides and nitrides, *Catal. Today* 15 (1992) 179–200.
- [35] Baowei Wang, Guozhong Ding, Yuguang Shang, Jing Lv, Haiyang Wang, Erdong Wang, Zhenhua Li, Xinbin Maa, Shaodong Qin, Q. Sun, Effects of MoO<sub>3</sub> loading and calcination temperature on the activity of the sulphur-resistant methanation catalyst MoO<sub>3</sub>/γ-Al<sub>2</sub>O<sub>3</sub>, *Appl. Catal. A: General* 431–432 (2012) 144–150.
- [36] S. Xie, K. Chen, A.T. Bell, E. Iglesia, Structural characterization of molybdenum oxide supported on zirconia, *J. Phys. Chem. B* 104 (2000) 10059–10068.
- [37] Komandur V.R. Chary, Kondakindi Rajender Reddy, J.W. Gurram Kishan, G. Mestl Niemantsverdriet, Structure and catalytic properties of molybdenum oxide catalysts supported on zirconia, *J. Catal.* 226 (2004) 283–291.
- [38] E.A. El-Sharkawy, A.S. Khder, A.I. Ahmed, Structural characterization and catalytic activity of molybdenum oxide supported zirconia catalysts, *Microporous Mesoporous Mater.* 102 (2007) 128–137.
- [39] K.D. Chen, S.B. Xie, E. Iglesia, A.T. Bell, Structure and properties of zirconia-supported molybdenum oxide catalysts for oxidative dehydrogenation of propane, *J. Catal.* 189 (2000) 421–430.
- [40] Thallada Bhaskar, Kondakindi Rajender Reddy, Chinthala Praveen Kumar, Mamidanna R.V.S. Murthy, K.V.R. Chary, Characterization and reactivity of molybdenum oxide catalysts supported on zirconia, *Appl. Catal. A: General* 211 (2001) 189–201.
- [41] K. Van der Borgh, K. Toch, V.V. Galvita, J.W. Thybaut, G.B. Marin, Information-driven catalyst design based on high-throughput intrinsic kinetics, *Catalysts* 5 (2015) 1948–1968.
- [42] I. Ascoop, V.V. Galvita, K. Alexopoulos, M.-F. Reyniers, P. Van Der Voort, V. Bliznuk, G.B. Marin, The role of CO<sub>2</sub> in the dehydrogenation of propane over WO<sub>x</sub>-VO<sub>x</sub>/SiO<sub>2</sub>, *J. Catal.* 335 (2016) 1–10.
- [43] R.J. Berger, E.H. Stitt, G.B. Marin, F. Kapteijn, J.A. Moulijn, Chemical reaction kinetics in practice, *Cattech* 5 (2001) 30–60.
- [44] J.J. Carberry, *Chemical Reaction Engineering*, ACS Audio Courses Washington (DC), 1980.
- [45] P.B. Weisz, C.D. Prater, Interpretation of measurements in experimental catalysis, *Adv. Catal.* (1954) 96–143.
- [46] D.E. Mears, Diagnostic criteria for heat transport limitations in fixed bed reactors, *J. Catal.* 20 (1971) 127–131.
- [47] D.E. Mears, The role of axial dispersion in trickle-flow laboratory reactors, *Chem. Eng. Sci.* 26 (1971) 1361–1366.
- [48] C.F. Chu, K.M. Ng, Flow in packed tubes with a small tube to particle diameter ratio, *AIChE J.* 35 (1989) 148–158.
- [49] E. Consortium, *Eurokin Spreadsheet for Assessment of Transport Limitations in Gas-solid Fixed Beds*, 2012.
- [50] K.V.R. Chary, G. Kishan, T. Bhaskar, H. Sivaraj, Structure and reactivity of vanadium oxide catalysts supported on anatase TiO<sub>2</sub>, *J. Phys. Chem. B* 102 (1998) 6792–6798.
- [51] K.V.R. Chary, T. Bhaskar, G. Kishan, K.R. Reddy, Characterization and reactivity of molybdenum oxide catalysts supported on niobia, *J. Phys. Chem. B* 105 (2001) 4392–4399.
- [52] P. Scherrer, Estimation of the size and internal structure of colloidal particles by means of röntgen, *Nachr. Ges. Wiss. Göttingen* 2 (1918) 96–100.
- [53] X. Zhang, D.H. He, Q.J. Zhang, Q. Ye, B.Q. Xu, Q.M. Zhu, Selective oxidation of methane to formaldehyde over Mo/ZrO<sub>2</sub> catalysts, *Appl. Catal. A- General* 249 (2003) 107–117.
- [54] L.M.S. Alves, F.S. Oliveira, B.S. de Lima, M.S. da Luz, A. Rebello, S.H. Masunaga, J.J. Neumeier, C. Giles, J.B. Leão, C.A.M. dos Santos, Evidence of phase transitions in MoO<sub>3</sub> single crystals, *J. Alloys Compd.* 705 (2017) 764–768.
- [55] K. Jacob, V. Saji, J. Gopalakrishnan, Y. Waseda, Thermodynamic evidence for phase transition in MoO<sub>2-s</sub>, *J. Chem. Thermodyn.* 39 (2007) 1539–1545.
- [56] Sara Boullousa-Eiras, Rune Lødeng, Håkon Bergem, Michael Stöcker, Lenka Hannevold, E.A. Blekkan, Catalytic hydrodeoxygenation (HDO) of phenol over supported molybdenum carbide, nitride, phosphide and oxide catalysts, *Catal. Today* 223 (2014) 44–53.
- [57] A. Calafat, L. Avilan, J. Aldana, The influence of preparation conditions on the surface area and phase formation of MoO<sub>3</sub>/ZrO<sub>2</sub> catalysts, *Appl. Catal. A: General* 201 (2000) 215–223.
- [58] K.V.R. Chary, K.R. Reddy, C.P. Kumar, Dispersion and reactivity of molybdenum oxide catalysts supported on titania, *Catal. Commun.* 2 (2001) 277–284.
- [59] J.E. De Vries, H.C. Yao, R.J. Baird, H.S. Gandhi, Characterization of molybdenum-platinum catalysts supported on γ-alumina by X-ray photoelectron spectroscopy, *J. Catal.* 84 (1983) 8–14.
- [60] M.J. Ledoux, C. Pham-Huu, H. Dunlop, J. Guille, Compared activities of platinum and high specific surface area Mo<sub>2</sub>C and WC catalysts for reforming reactions, *J. Catal.* 134 (1992) 383–398.
- [61] J.G. Choi, L.T. Thompson, XPS study of as-prepared and reduced molybdenum oxides, *Appl. Surface Sci.* 93 (1996) 143–149.
- [62] N.K. Nag, A comparative study on the dispersion and carrier-catalyst interaction of molybdenum oxides supported on various oxides by electron spectroscopy for chemical analysis, *J. Phys. Chem.* 91 (1987) 2324–2327.
- [63] Y. Holl, R. Touroude, G. Maire, A. Muller, P.A. Engelhard, J. Grosmani, Skeletal isomerization of hydrocarbons on molybdenum catalysts, *J. Catal.* 104 (1987) 202–210.
- [64] D.O. Scanlon, G.W. Watson, D. Payne, G. Atkinson, R. Egdell, D. Law, Theoretical and experimental study of the electronic structures of MoO<sub>3</sub> and MoO<sub>2</sub>, *J. Phys. Chem. C* 114 (2010) 4636–4645.
- [65] J. Baltrusaitis, B. Mendoza-Sanchez, V. Fernandez, R. Veenstra, N. Dukstiene, A. Roberts, N. Fairley, Generalized molybdenum oxide surface chemical state XPS determination via informed amorphous sample model, *Appl. Surface Sci.* 326 (2015) 151–161.
- [66] M.A. Gonzalez-Borja, D.E. Resasco, Anisole and guaiacol hydrodeoxygenation over monolithic Pt-Sn catalysts, *Energy Fuels* 25 (2011) 4155–4162.
- [67] A. Pandurangan, Vapor phase hydrodeoxygenation of anisole over ruthenium and nickel supported mesoporous aluminosilicate, *Green Chem.* (2016).
- [68] T.R. Viljava, R.S. Komulainen, A.O.I. Krause, Effect of H<sub>2</sub>S on the stability of CoMo/Al<sub>2</sub>O<sub>3</sub> catalysts during hydrodeoxygenation, *Catal. Today* 60 (2000) 83–92.
- [69] X. Zhu, L.L. Lobban, R.G. Mallinson, D.E. Resasco, Bifunctional transalkylation and hydrodeoxygenation of anisole over a Pt/HBeta catalyst, *J. Catal.* 281 (2011) 21–29.
- [70] C.V. Loricera, B. Pawelec, A. Infantes-Molina, M.C. Alvarez-Galvan, R. Huirache-Acuna, R. Nava, J.L.G. Fierro, Hydrogenolysis of anisole over mesoporous sulfided CoMoW/SBA-15(16) catalysts, *Catal. Today* 172 (2011) 103–110.
- [71] Kelun Li, Rijie Wang, J. Chen, Hydrodeoxygenation of anisole over silica-supported Ni<sub>2</sub>P, MoP, and NiMoP catalysts, *Energy Fuels* 25 (2011) 854–863.
- [72] R. Lødeng, C. Ranga, T. Rajkhowa, V.I. Alexiadis, H. Björkan, S. Chytil, I.H. Svernum, J. Walmley, J.W. Thybaut, Hydrodeoxygenation of phenolics in liquid phase over supported MoO<sub>3</sub> and carburized analogues, *Biomass Convers. Bioref.* (2017) 1–17.
- [73] J.E. Peters, J.R. Carpenter, D.C. Dayton, Anisole and guaiacol hydrodeoxygenation reaction pathways over selected catalysts, *Energy Fuels* 29 (2015) 909–916.
- [74] V.N. Bui, D. Laurenti, P. Afanasiev, C. Geantet, Hydrodeoxygenation of guaiacol with CoMo catalysts. Part I: Promoting effect of cobalt on HDO selectivity and activity, *Appl. Catal. B: Environ.* 101 (2011) 239–245.
- [75] W.-S. Lee, A. Kumar, Z. Wang, A. Bhan, Chemical titration and transient kinetic studies of site requirements in Mo<sub>2</sub>C-catalyzed vapor phase anisole hydrodeoxygenation, *ACS Catal.* 5 (2015) 4104–4114.
- [76] H. Wang, M. Feng, B. Yang, Catalytic hydrodeoxygenation of anisole: an insight into the role of metals in transalkylation reactions in bio-oil upgrading, *Green Chem.* 19 (2017) 1668–1673.
- [77] M. Saidi, H.R. Rahimpour, B. Rahzani, P. Rostami, B.C. Gates, M.R. Rahimpour, Hydroprocessing of 4-methylanisole as a representative of lignin-derived bio-oils catalyzed by sulphided CoMo/γ-Al<sub>2</sub>O<sub>3</sub>: a semi-quantitative reaction network, *Canad. J. Chem. Eng.* 94 (2016) 1524–1532.
- [78] A. Van Hengstum, J. Van Ommen, H. Bosch, P. Gellings, Preparation of supported vanadium and molybdenum oxide catalysts using metal acetylacetonate complexes, *Appl. Catal.* 5 (1983) 207–217.
- [79] N.K. Nag, Characterization of MoAl<sub>2</sub>O<sub>3</sub> catalysts by low-temperature oxygen chemisorption, *J. Catal.* 92 (1985) 432–437.
- [80] D.R. Moberg, T.J. Thibodeau, F.G. Amar, B.G. Frederick, Mechanism of hydrodeoxygenation of acrolein on a cluster model of MoO<sub>3</sub>, *J. Phys. Chem. C* 114 (2010) 13782–13795.
- [81] D. Mei, A.M. Karim, Y. Wang, Density functional theory study of acetaldehyde hydrodeoxygenation on MoO<sub>3</sub>, *J. Phys. Chem. C* 115 (2011) 8155–8164.
- [82] K. Murugappan, C. Mukarakate, S. Budhi, M. Shetty, M.R. Nimlos, Y. Román-Leshkov, Supported molybdenum oxides as effective catalysts for the catalytic fast pyrolysis of lignocellulosic biomass, *Green Chem.* (2016).